g-Anisotropy

The g-factor (or g-value) characterizes the position of the EPR resonance line in an EPR spectrum. The g-value of the free electron (having no orbital angular momentum $L = 0$) is ~ 2.0023. Paramagnetic systems with highly delocalized electrons show a g-value very close to this value which always indicates a very small coupling of spin and orbital moments (spin-orbit coupling, SOC). However, g often differs from this value if the contribution of SOC is *not* negligible. In this case, interaction of excited states with the electron ground state admixes orbital angular momentum L to the ground state that couple to the electron spin S. As a result, the g-value is no longer isotropic and the splitting of the Zeeman levels depends further on the environment of the electron spin (e.g. the symmetry of the crystal field or the orientation of the system within the magnetic field). Therefore, the g-values are a 'fingerprint' of the electronic environment of the observed electron spin, analogous to the chemical shift in nuclear magnetic resonance.

The 'effective field' B_{eff} experienced by the electron spin is a superposition of the internal and external fields and the energy of this anisotropic interaction is given by:

$$H_{EZ} = g_e \frac{\mu_B}{\hbar} \boldsymbol{B}_{eff} \boldsymbol{S} = \frac{\mu_B}{\hbar} \boldsymbol{B}_0^T \, \mathbf{g} \, \boldsymbol{S}, \tag{2.7a}$$

$$= \frac{\mu_B}{\hbar} \left(B_{0,x}\, B_{0,y}\, B_{0,z}\right) \begin{pmatrix} g_{xx} & & \\ & g_{yy} & \\ & & g_{zz} \end{pmatrix} \begin{pmatrix} S_x \\ S_y \\ S_z \end{pmatrix} \tag{2.7b}$$

The orientation dependent Zeeman interaction is expressed by a (3x3) **g** interaction matrix, that can be represented in its principal axes system (PAS) by a diagonal matrix (eq. (2.7a)), where (x, y, z) is the PAS and g_{xx}, g_{yy} and g_{zz} are the principal values of the **g**-matrix, commonly denoted as the g-tensor.

For an axially symmetric **g**-matrix, the two identical elements are combined to $g_{xx} = g_{yy} = g_\perp$ and the remaining element is denoted as $g_\parallel$. Per definition $g_\perp$ is perpendicular and $g_\parallel$ is parallel to the unique axis of the **g**-matrix. In liquid solution when molecular rotation about the three axes is fast, the g-anisotropy is averaged to the isotropic g_{iso}-value that can be calculated from the **g**-tensor according to eq.(2.8). Often used definitions related to the **g**-tensor are the anisotropy Δg and the asymmetry η.

$$g_{\text{iso}} = \frac{1}{3}(g_{xx} + g_{yy} + g_{zz}) = \frac{1}{3} trace(\mathbf{g}) \tag{2.8}$$

$$\Delta g = g_{zz} - g_{iso} \qquad \eta = \frac{g_{yy} - g_{xx}}{\Delta g}$$

On the basis of the element pattern of the **g**-matrix several cases of matrix symmetry can be distinguished, namely isotropic, axial, or rhombic. Examples for powder EPR spectra for different **g**-anisotropies are shown in Figure 2.3.

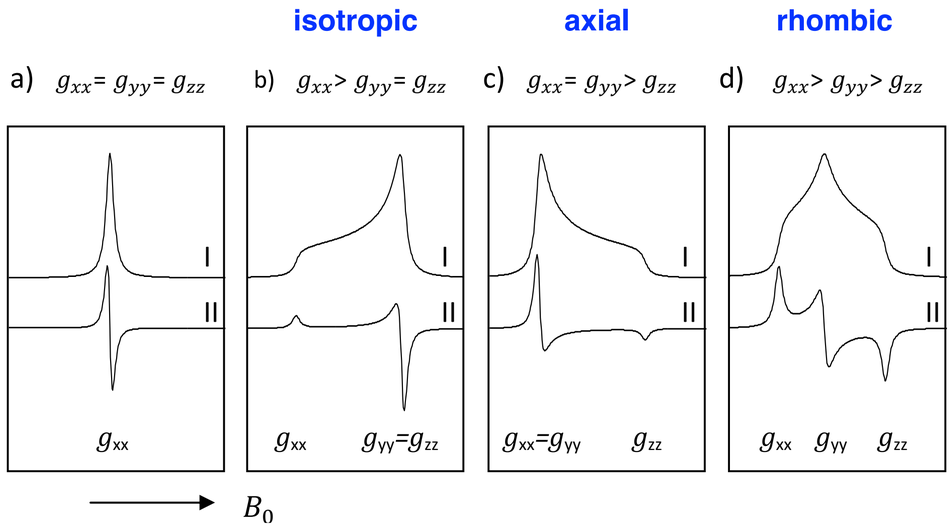

Figure 2.3 Simulated EPR spectra in absorption (I) and first derivative (II) mode for isotropic (a), axial (b,c) and rhombic (d) g-tensor.

The anisotropy of $\mathbf{g}$ can be measured by recording the EPR spectra of a *single crystal* (where the molecules are in fixed orientations) by rotating the crystal in the magnetic field with respect to three orthogonal axes in the sample and transforming the sample frame (that may be given by e.g. the crystal symmetry) into the molecular frame (the PAS of the $\mathbf{g}$-matrix), which can be further transformed into the laboratory frame (where the z-axis is collinear the direction of B_0). The EPR spectrum of a *powder* is a supersposition of EPR lines of randomly oriented microcrystals. The same is true for paramagnets in *glassy matrices*. However, the $\mathbf{g}$-anisotropy can be measured even for such samples (see Section 2.9.4).

For B_0 pointing along one of the principal axes, the spin vector $\boldsymbol{S}$ is quantized along B_0 and the resonant field value can easily be calculated from the resonance (eq. (2.5). For an arbitrary direction of B_0 the $\mathbf{g}$ -matrix can be expressed as a symmetric tensor and three Euler angles α, β and γ describing their orientation relative to each other.

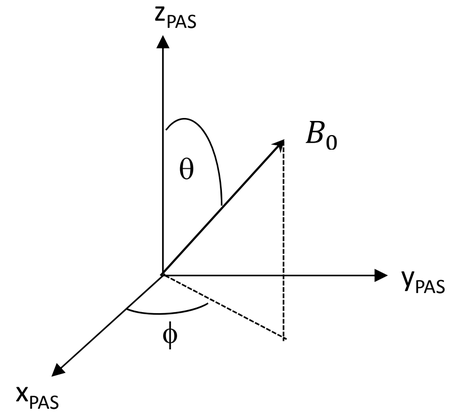

Figure 2.4 The orientation of the magnetic field vector $B_0$with respect to the $\mathbf{g}$-tensor principal axes system is defined by the polar angles θ and ϕ.

Note, that the orientation of the PAS with respect to B_0 is usually specified via the polar angles θ, ϕ or the direction cosines and the transformation of an interaction tensor into the laboratory frame $R(\theta, \phi)$ is also an Euler rotation where only *two* angles are required (in the laboratory frame no distinction is made between the x and y axes). Within this nomenclature θ denotes the Euler rotation about the y-axis, which is $R_y(\theta)$ and corresponds to $\beta = 0$.

g-Anisotropy

The g-anisotropy depends on the spin orbit coupling.
Perturbation theory gives:

mixing of molecular orbitals

$$g_{ij} = g_e + 2\lambda \sum_n \frac{\langle \psi_0 | \hat{L}_i | \psi_n \rangle \langle \psi_n | \hat{L}_j | \psi_0 \rangle}{E_0 - E_n}$$

spin-orbit coupling parameter

General trends:

- Radicals with light elements e.g. C, H, O, N .
  - Weak spin orbit coupling
  - Small g-anisotropy and signals near g=2.0023.
- Transition metals
  - Moderate to strong spin-orbit coupling
  - Larger g-anisotropy
  - g-anisotropy depends on the electronic configuration and the symmetry of the ligand field.

A - the hyperfine splitting

- The unpaired electron, which gives us the EPR spectrum, is very sensitive to local fields in its surroundings.
- Local fields arising from magnetic nuclei are *permanent and independent of H, because of (a · S · I)*
- Interaction with neighboring nuclear magnetic dipoles gives the *nuclear hyperfine interaction* and *hyperfine splitting A*
- Corresponds to the NMR coupling constant J *(interaction between nuclei containing spin)*
- For several equivalent nuclei n, $(2n_M I_M + 1)$ transitions are observed for a nucleus M with a spin I
- The relative intensities are given by Pascal's triangle for I = ½

1
1 1
1 2 1
1 3 3 1
1 4 6 4 1
1 5 10 10 5 1

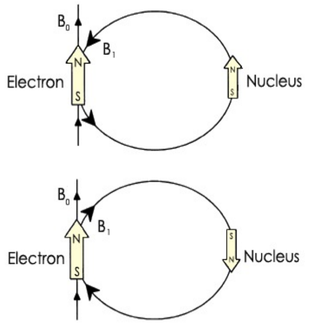

Hyperfine coupling constants have two contributions:

Fermi contact $$a_{iso} = \frac{2}{3}\frac{\mu_0 \beta_e \beta_n}{h} g_e g_n |\psi(0)|^2$$

electron spin density at the nucleus

Dipolar coupling $$a_{dipolar} = \frac{\mu_0}{4\pi}\frac{\beta_e \beta_n}{h} g_e g_n \left\langle \frac{3\cos^2\theta - 1}{r^3} \right\rangle$$

in solution this average is zero

In general simulations are necessary to obtain the hyperfine coupling constants

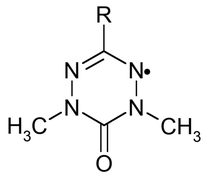

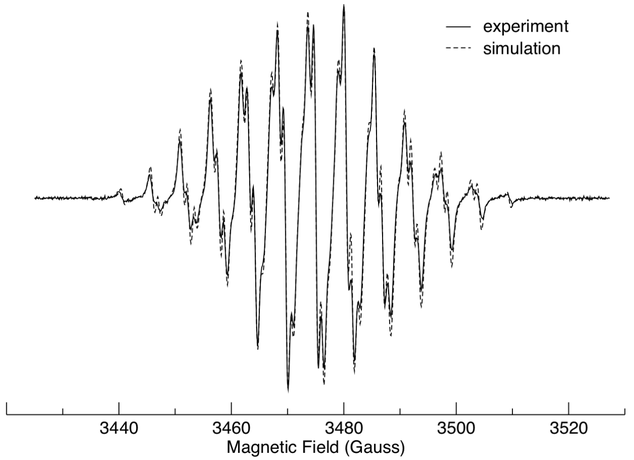

Two different physical effects can contribute to the hf interaction: the anisotropic *dipole-dipole* interaction (acting through space solely) and the isotropic *Fermi-contact* ('trough bond') interaction. These can be classified according to the 'effective distance' of the electron to the nuclear spin into two regions, one inside and one outside the nuclear volume. Quantum mechanics allows an electron to enter the volume occupied by nuclei, whereas outside the nuclear volume the hf field is the classical field of magnetic dipoles.

The dipole-dipole interaction between two spins can be derived from the classical physics, where the spins are treated as bar magnets, interacting in an outer magnetic field. Additionally, each bar magnet creates a magnetic field, which in turn influences the local field at the other nuclei's place. The dipolar interaction Hamiltonian is derived from the classical energy expression for two interacting dipoles μ_1 and μ_2 separated by the distance r by replacing μ_i by the corresponding electron or nuclear spin that is $\boldsymbol{\mu_e} = g\mu_B \boldsymbol{S}$ for the electron and $\boldsymbol{\mu_e} = g_N\mu_N \boldsymbol{I}$ for the nuclear spin, which leads to the expression:

$$H_{dd} = \frac{\mu_0}{4\pi\hbar} \cdot \frac{1}{r^3} g g_N \mu_B \mu_N \left[\boldsymbol{SI} - \frac{3(\boldsymbol{S}\mathbf{r})(\boldsymbol{I}\mathbf{r})}{r^2} \right] = \boldsymbol{S}^T \mathbf{T} \boldsymbol{I} \qquad (2.12)$$

In eq. (2.12) μ_0 is the vacuum permeability ($4\pi \cdot 10^{-7}$ NA^{-2}) and r the distance between the two spins connected by the vector $\mathbf{r}$. $\mathbf{T}$ is the traceless dipolar hyperfine coupling tensor. The dipolar interaction depends on the orientation of the connecting vector $\mathbf{r}$ with respect to the outer magnetic field and is thus anisotropic. The dipolar interaction is expected to be the main contribution to the overall hf interaction when the electron spin is located in an orbital with a nodal point at the nucleus (which includes all orbitals except s-orbitals) and a symmetry of the full spin system that is lower than cubic. The dipolar interaction is averaged out for rapidly tumbling paramagnets, as it is usual for liquid solution at ambient temperatures or above. In the solid state (e.g. frozen solution) the dipolar contribution to the hf field is important and can be used to calculate the distance between the electron and nuclear spin.

The Fermi-contact interaction is isotropic and a consequence of a finite amplitude $|\Psi(0)|^2$ of the electronic wave function at the nucleus. Hence, this mechanism works through direct contact of the unpaired electron and the nucleus and the energy of this interaction is given by:

$$H_{fc} = \frac{2\mu_0}{3\hbar} g g_N \mu_B \mu_N |\Psi(0)|^2 = a_{iso} \boldsymbol{S}^T \boldsymbol{I}$$

Thus, the overall energy of the hyperfine interaction between electron and nuclear magnetic moments is given by the sum of the isotropic and anisotropic hf interactions in the spin Hamiltonian:

$$H_{HF} = H_{fc} + H_{dd} = \boldsymbol{S}^T \mathbf{A} \boldsymbol{I} \qquad (2.14)$$

$\mathbf{A}$ is the hyperfine interaction matrix, that is represented in the PAS:

$$\mathbf{A} = \begin{bmatrix} A_{xx} & & \\ & A_{yy} & \\ & & A_{zz} \end{bmatrix} = \mathbf{1} a_{iso} + \begin{bmatrix} T_{xx} & & \\ & T_{yy} & \\ & & T_{zz} \end{bmatrix} \qquad (2.15)$$

For *axial* symmetry of the dipolar interaction tensor $\mathbf{T}$, the principal values would be $T_{xx} = T_{yy} = -T_\perp$ and $T_{zz} = 2T_\perp = T_\parallel$. For electron-nuclear distances r greater than 0.25 nm, and when spin delocalization is negligible, $T_\perp$ can be described by the point-dipole approximation [25]:

$$T_\perp = \frac{\mu_0 \rho}{4\pi\hbar} \cdot \frac{g\mu_B g_N \mu_N}{r^3} \qquad (2.16)$$

where $\rho = |\Psi(0)|^2$ is the electron spin density. This relation in eq. (2.16) is important because it allows a straightforward interpretation of the anisotropic hf interaction in terms of distances between the electron and the hyperfine coupled nucleus. Alternatively, when the distance is known, it can provide the spin density ρ on the nucleus.

Zero-field Splitting

If more than one interchangeable electron is present in the system, the individual electron spins S_i are coupled to form a total spin of $S = \sum S_i$, where each electron contributes to S with the value ½. As a result, the two state system of the single electron is converted to a $(2S + 1)$ manifold even in absence of an external magnetic field. Since transitions may then occur at zero magnetic field this interaction is called zero-field splitting. The Hamiltonian of this interaction is

$$H_{\mathrm{ZFS}} = \boldsymbol{S}^T \mathbf{D} \boldsymbol{S}, \qquad (2.9)$$

with $\mathbf{D}$ the symmetric and traceless zero-field interaction tensor. This 'fine-structure' term vanishes completely for cubic symmetry of the spin system.

$$\boldsymbol{D} = \begin{pmatrix} -\frac{1}{3}D + E & 0 & 0 \\ 0 & -\frac{1}{3}D - E & 0 \\ 0 & 0 & \frac{2}{3}D \end{pmatrix}$$

Anisotropy in g and A

The ability of EPR to obtain useful information from amorphous (glassy) and polycrystalline (powders) as well as from single crystal materials has attracted much biology and biochemistry research

Usually : g_X, g_Y, g_Z are not all equal, so g is anisotropic. Same for A_X, A_Y, A_Z.

For EPR the local symmetry at an unpaired electron center is categorised as :

- *Cubic*. If x = y = z is cubic (*cubal, octahedral, tetrahedral*) No anisotropy in g and A.
- *Uniaxial (Axial)*. If x = y, and z is unique.

Linear rotation symmetry (at least 3-fold). Two principal values each for g and A. For an arbitrary orientation:

$$g_\theta^2 = g_\perp^2 \sin^2\theta + g_{II}^2 \cos^2\theta$$

- *Rhombic*. Three unequal components for g and A

For an arbitrary orientation:

$$g^2 = g_{XX}^2 \sin^2\theta \cos^2\phi + g_{YY}^2 \sin^2\theta \sin^2\phi + g_{ZZ}^2 \cos^2\phi$$

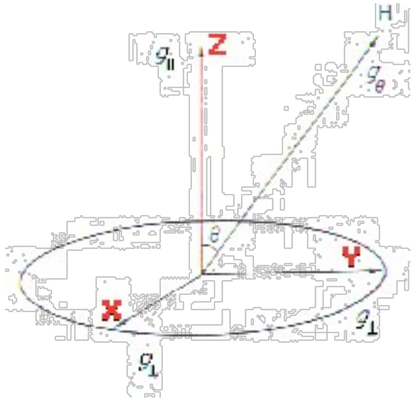

⑥ Principle Axes

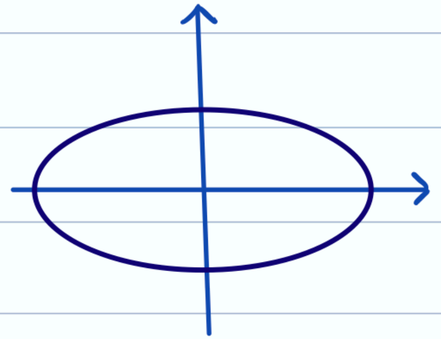

$$\rightarrow \quad x^2 + 4y^2 = 1 = (x, y)\begin{pmatrix} 1 & 0 \\ 0 & 4 \end{pmatrix}\begin{pmatrix} x \\ y \end{pmatrix}$$

$\langle r|$ — B — $|r\rangle$

$$= \langle r \mid B \mid r \rangle$$

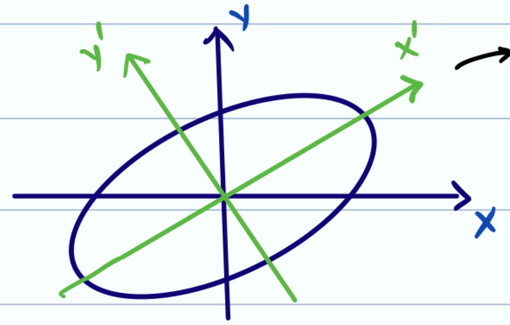

$$\rightarrow \quad \frac{5}{2}x^2 - 3xy + \frac{5}{2}y^2 = 1 = \langle r| \begin{pmatrix} 5/2 & -3/2 \\ -3/2 & 5/2 \end{pmatrix} |r\rangle$$

A

→ To Find principle axes

$$\langle r|A|r\rangle = \langle r|R\,\tilde{R}^{-1}AR\,\tilde{R}^{-1}|r\rangle = \langle r'|\begin{pmatrix} 1 & 0 \\ 0 & 4 \end{pmatrix}|r'\rangle$$

$\langle r'|$ — diag — $|r'\rangle$

$$= \langle r' \mid B \mid r' \rangle$$

new coord. $= \begin{pmatrix} x' \\ y' \end{pmatrix}$

Construction of g matrix

$$\hat{\mathcal{H}} = \beta_e [B_X \quad B_Y \quad B_Z] \cdot \begin{bmatrix} g_\perp & 0 & 0 \\ 0 & g_\perp & 0 \\ 0 & 0 & g_\parallel \end{bmatrix} \cdot \begin{bmatrix} \hat{S}_X \\ \hat{S}_Y \\ \hat{S}_Z \end{bmatrix}$$

$$= \beta_e \mathbf{B}^{\mathrm{T}} \cdot g \cdot \hat{\mathbf{S}}$$

magnetic moment

$$\hat{\boldsymbol{\mu}} = \beta_e \mathbf{g} \cdot \hat{\mathbf{S}}$$

which is taken to interact with the field $\mathbf{B}$ (see Eqs. 1.14).

Alternatively, the product $\mathbf{B}^{\mathrm{T}} \cdot \mathbf{g}$ in Eq. 4.4*c* may be regarded as a vector resulting from a transformation of the actual field $\mathbf{B}$ to an effective field

$$\mathbf{B}_{\mathrm{eff}} = \mathbf{g}^{\mathrm{T}} \cdot \mathbf{B} / g_e \tag{4.9a}$$

or equivalently

$$\mathbf{B}_{\mathrm{eff}}{}^{\mathrm{T}} \equiv \mathbf{B}^{\mathrm{T}} \cdot \mathbf{g} / g_e \tag{4.9b}$$

The magnitude of the effective field is given by

$$B_{\mathrm{eff}} = [(\mathbf{g}^{\mathrm{T}} \cdot \mathbf{B})^{\mathrm{T}} \cdot (\mathbf{g}^{\mathrm{T}} \cdot \mathbf{B})]^{1/2} / g_e \tag{4.10a}$$

$$= [\mathbf{B}^{\mathrm{T}} \cdot \mathbf{g} \cdot \mathbf{g}^{\mathrm{T}} \cdot \mathbf{B})]^{1/2} / g_e \tag{4.10b}$$

$$= \left\{ [\mathbf{n}^{\mathrm{T}} \cdot (\mathbf{g} \cdot \mathbf{g}^{\mathrm{T}}) \cdot \mathbf{n})]^{1/2} / g_e \right\} B \tag{4.10c}$$

$\sqrt{\langle n | g \rangle \langle g | n \rangle}$

$$\mathbf{n} = \mathbf{B}/B = \begin{bmatrix} c_x \\ c_y \\ c_z \end{bmatrix}$$

$$\mathbf{n}^{\mathrm{T}} = \begin{bmatrix} \sin\theta\cos\phi & \sin\theta\sin\phi & \cos\theta \end{bmatrix}$$

is the unit vector along **B**. In concert with Eq. 1.22*b*, we define

$$g = [\mathbf{n}^{\mathrm{T}} \cdot (\mathbf{g} \cdot \mathbf{g}^{\mathrm{T}}) \cdot \mathbf{n})]^{1/2} \qquad \mathbf{n}^{\mathrm{T}} = \begin{bmatrix} \sin\theta\cos\phi & \sin\theta\sin\phi & \cos\theta \end{bmatrix}$$

We adopt the definition $\mathbf{gg} \equiv \mathbf{g} \cdot \mathbf{g}^{\mathrm{T}}$, and now explore some of the properties of this parameter matrix.[2] Even if **g** is asymmetric, **gg** is always symmetric. Thus we need write explicitly only the diagonal and upper off-diagonal elements. In any arbitrary cartesian coordinate system *x*, *y*, *z* fixed in the crystal, **gg** is not diagonal, so that

$$g^2 = \begin{bmatrix} c_x & c_y & c_z \end{bmatrix} \cdot \begin{bmatrix} (\mathbf{gg})_{xx} & (\mathbf{gg})_{xy} & (\mathbf{gg})_{xz} \\ & (\mathbf{gg})_{yy} & (\mathbf{gg})_{yz} \\ & & (\mathbf{gg})_{zz} \end{bmatrix} \cdot \begin{bmatrix} c_x \\ c_y \\ c_z \end{bmatrix} \tag{4.15}$$

Following the procedure outlined in Section A.5.2, we now turn to the general case of the calculation of matrix **gg** from sets of measurements, for which

$$\begin{aligned} g^2 = {} & (\mathbf{gg})_{xx}\sin^2\theta\cos^2\phi + 2(\mathbf{gg})_{xy}\sin^2\theta\cos\phi\sin\phi \\ & + (\mathbf{gg})_{yy}\sin^2\theta\sin^2\phi + 2(\mathbf{gg})_{xz}\cos\theta\sin\theta\cos\phi \\ & + 2(\mathbf{gg})_{yz}\cos\theta\sin\theta\sin\phi + (\mathbf{gg})_{zz}\cos^2\theta \end{aligned} \tag{4.16a}$$

The $(\mathbf{gg})_{ij}$ elements can be determined from experiment by successive rotations of the crystal with **n** fixed (or alternatively rotations of the field, i.e., of **n**, with the crystal fixed) in the xz, yz, and xy planes. For the xz plane ($\phi = 0$), if θ is the angle between **B** and the z axis, $c_x = \sin\,\theta$, $c_y = 0$, and $c_z = \cos\,\theta$. Then

$$g^2 = [\sin\theta \quad 0 \quad \cos\theta] \cdot \begin{bmatrix} (\mathbf{gg})_{xx} & (\mathbf{gg})_{xy} & (\mathbf{gg})_{xz} \\ & (\mathbf{gg})_{yy} & (\mathbf{gg})_{yz} \\ & & (\mathbf{gg})_{zz} \end{bmatrix} \cdot \begin{bmatrix} \sin\theta \\ 0 \\ \cos\theta \end{bmatrix} \tag{4.16b}$$

and

$$g^2 = (\mathbf{gg})_{xx}\sin^2\theta + 2(\mathbf{gg})_{xz}\sin\theta\cos\theta + (\mathbf{gg})_{zz}\cos^2\theta \tag{4.16c}$$

Similarly, for rotation in the yz plane ($\phi = 90^\circ$), $c_x = 0$, $c_y = \sin\,\theta$, and $c_z = \cos\,\theta$ so that

$$g^2 = (\mathbf{gg})_{yy}\sin^2\theta + 2(\mathbf{gg})_{yz}\sin\theta\cos\theta + (\mathbf{gg})_{zz}\cos^2\theta \tag{4.17}$$

Likewise, for rotation in the xy plane ($\theta = 90^\circ$), $c_x = \cos\,\phi$, $c_y = \sin\,\phi$, and $c_z = 0$ and hence

$$g^2 = (\mathbf{gg})_{xx}\cos^2\phi + 2(\mathbf{gg})_{xy}\sin\phi\cos\phi + (\mathbf{gg})_{yy}\sin^2\phi \tag{4.18}$$

$$\underbrace{\begin{bmatrix} C_{Xx} & C_{Xy} & C_{Xz} \\ C_{Yx} & C_{Yy} & C_{Yz} \\ C_{Zx} & C_{Zy} & C_{Zz} \end{bmatrix}}_{\mathbf{C}} \cdot \underbrace{\begin{bmatrix} (gg)_{xx} & (gg)_{xy} & (gg)_{xz} \\ & (gg)_{yy} & (gg)_{yx} \\ & & (gg)_{zz} \end{bmatrix}}_{\mathbf{gg}} \cdot \underbrace{\begin{bmatrix} C_{Xx} & C_{Yx} & C_{Zx} \\ C_{Xy} & C_{Yy} & C_{Zy} \\ C_{Xz} & C_{Yz} & C_{Zz} \end{bmatrix}}_{\mathbf{C}^{\mathrm{T}}}$$

$$= \underbrace{\begin{bmatrix} (gg)_X & 0 & 0 \\ & (gg)_Y & 0 \\ & & (gg)_Z \end{bmatrix}}_{\mathbf{d_{gg}}} \qquad (4.19)$$

Idea: single crystal ==> obtain matrix gg ==> solve for C matrix ==> diagonal matrix obtained.

Rotation matrix

$$R = \begin{pmatrix} \cos\alpha\cos\beta\cos\gamma - \sin\alpha\sin\gamma & \sin\alpha\cos\beta\cos\gamma + \cos\alpha\sin\gamma & -\sin\beta\cos\gamma \\ -\cos\alpha\cos\beta\sin\gamma - \sin\alpha\cos\gamma & -\sin\alpha\cos\beta\sin\gamma + \cos\alpha\cos\gamma & \sin\beta\sin\gamma \\ \cos\alpha\sin\beta & \sin\alpha\sin\beta & \cos\beta \end{pmatrix}$$

Single crystal EPR

The orientation dependence of the spectra can be studied in single crystals

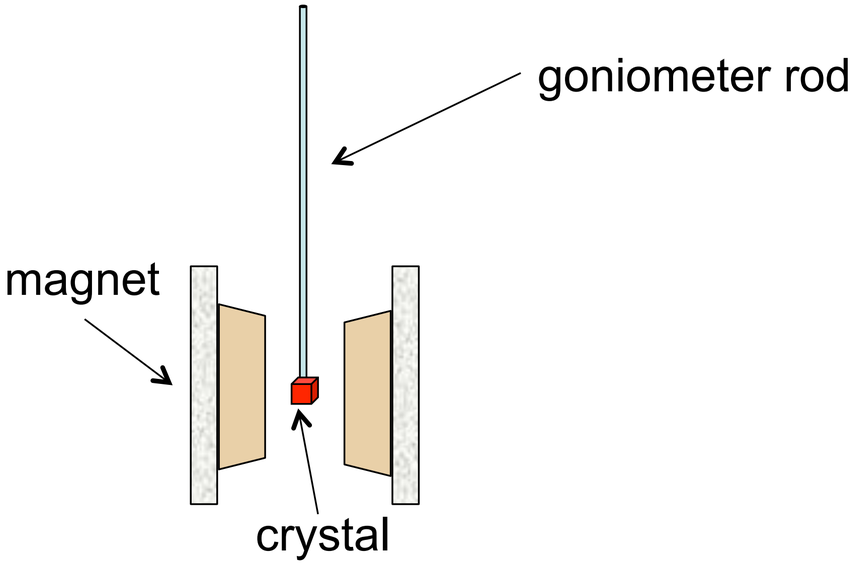

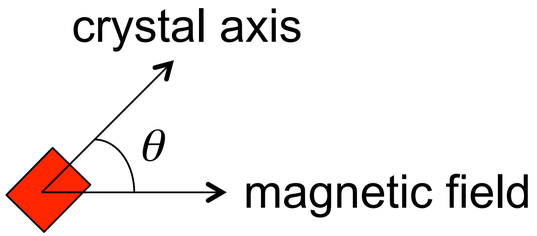

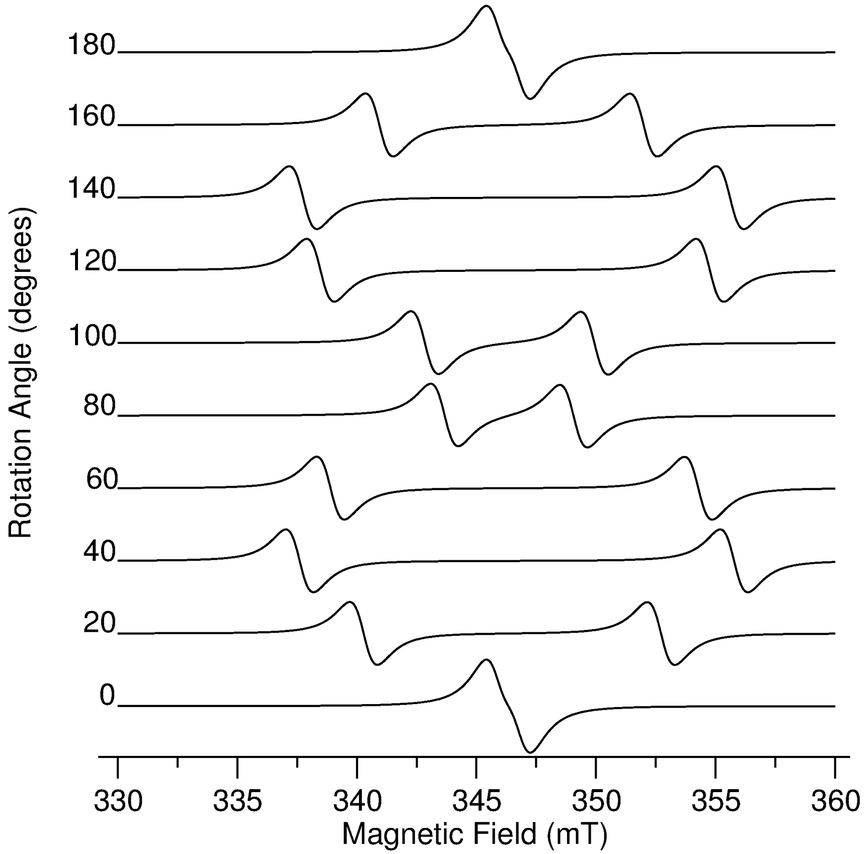

Single crystal EPR

The g-values of the lines are fitted to the equation:

$$g_{eff}^2 = g_{aa}^2 \cos^2\theta + 2g_{ab}^2 \cos\theta \sin\theta + g_{bb}^2 \sin^2\theta$$

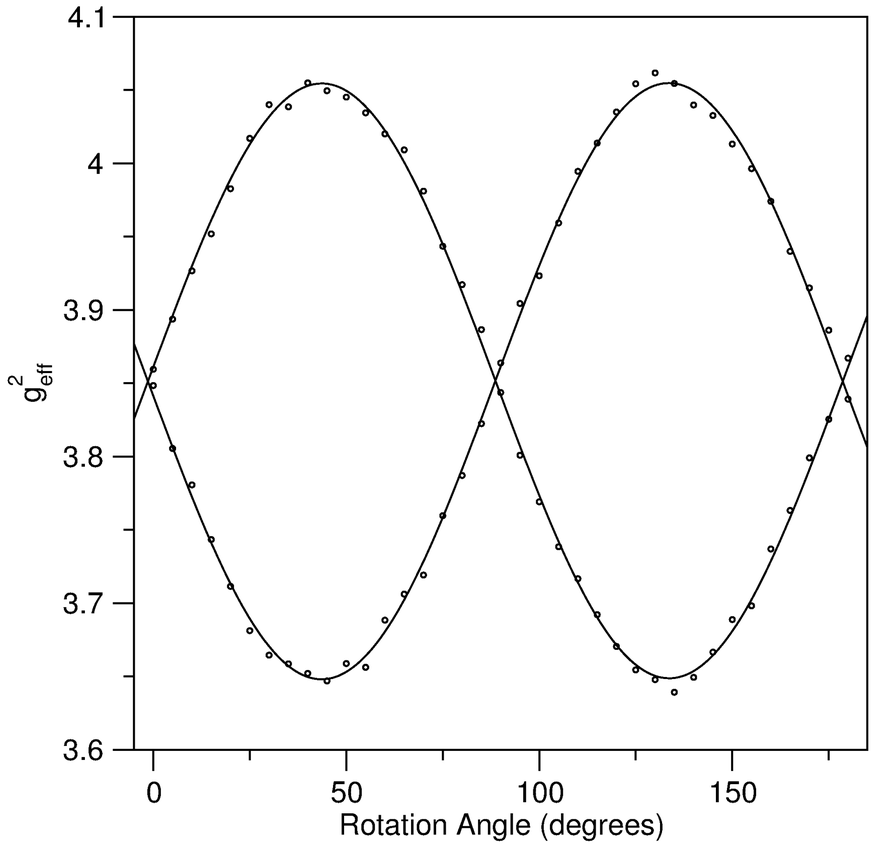

Rotation in 3 independent planes gives values of

$$g_{aa}^2, g_{bb}^2, g_{cc}^2, g_{ab}^2, g_{ac}^2, g_{bc}^2$$

Single crystal EPR

The g-tensor is then diagonalized numerically

$$\begin{bmatrix} g_{aa}^2 & g_{ab}^2 & g_{ac}^2 \\ g_{ab}^2 & g_{bb}^2 & g_{bc}^2 \\ g_{ac}^2 & g_{bc}^2 & g_{cc}^2 \end{bmatrix} \longrightarrow \begin{bmatrix} g_{xx}^2 & 0 & 0 \\ 0 & g_{yy}^2 & 0 \\ 0 & 0 & g_{zz}^2 \end{bmatrix}$$

this gives the principal g-values g_{xx}, g_{yy} and g_{zz} .

The diagonalization is achieved by the transformation:

$$\boldsymbol{U}\boldsymbol{g}^2\boldsymbol{U}^{-1} = \boldsymbol{g}_{diagonal}^2$$

The tranformation matrix $\boldsymbol{U}$ gives the orientation of the principal axes x,y,z in the crystal axis system a,b,c

Example Iron Sulfur Clusters in Photosystem I:

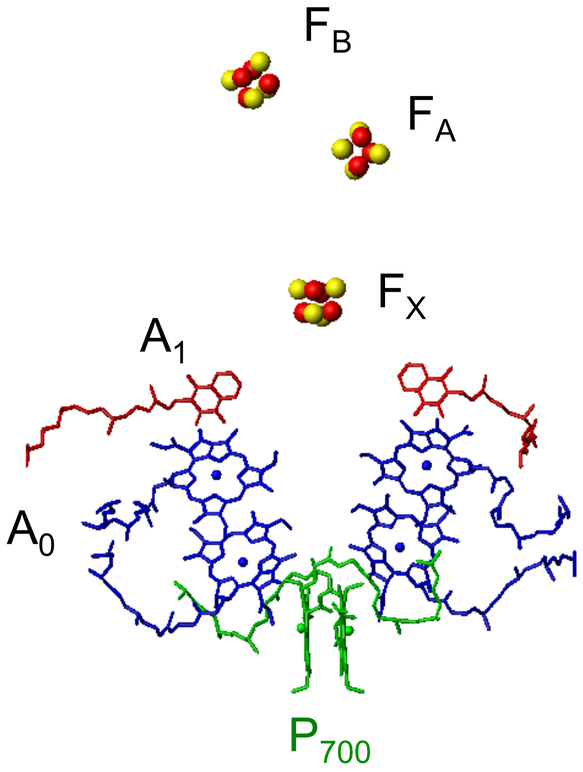

Rotation about *c*-axis

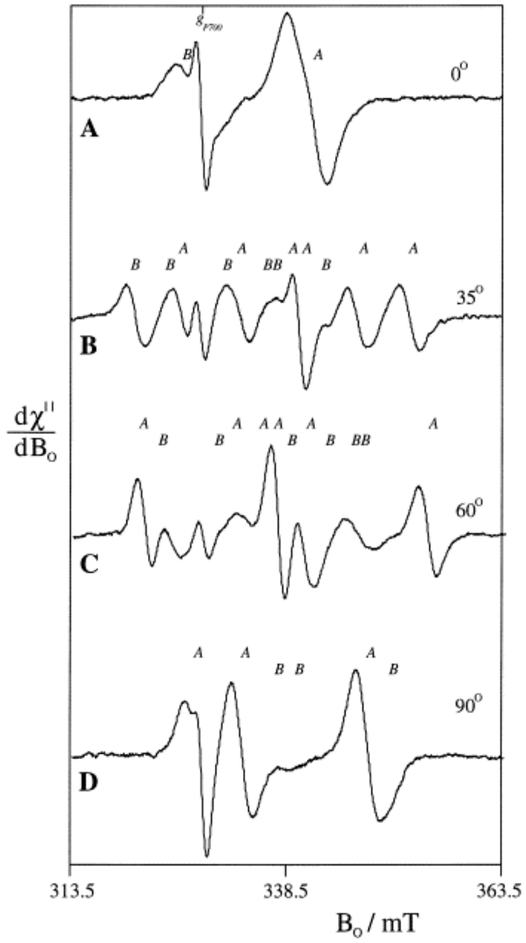

Kamlowski *et al* Biochim. Biophys. Acta 1319 (1997) 185–198

When only g is taken into consideration …

g_x=2.0091, g_y=2.0061, g_z=2.0023

The field shift between the X- and Z- orientations is

$\Delta H = h\nu/g_x\beta - h\nu/g_z\beta \cong h\nu\Delta g/4\beta \sim 11G$

$$\Delta E = h\nu = g\beta H$$

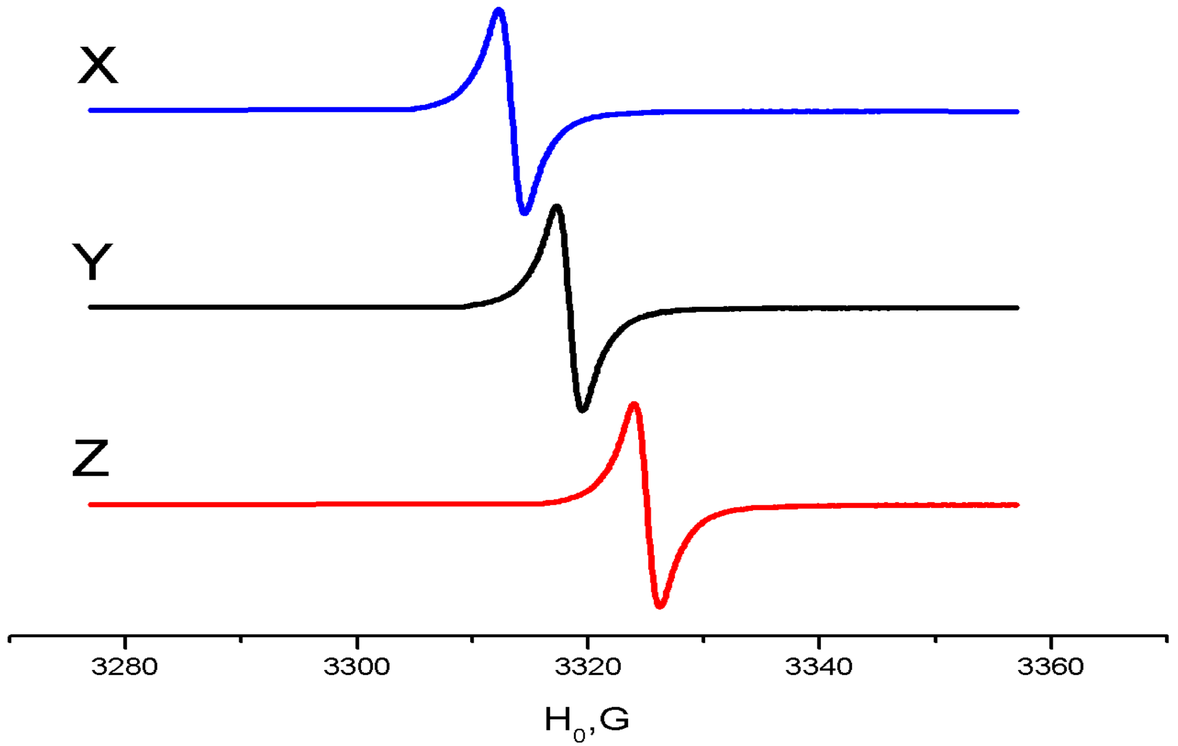

g_x=2.0091, g_y=2.0061, g_z=2.0023

I=1/2, A_x= 6.2, A_y = 6.3, A_z=33.6

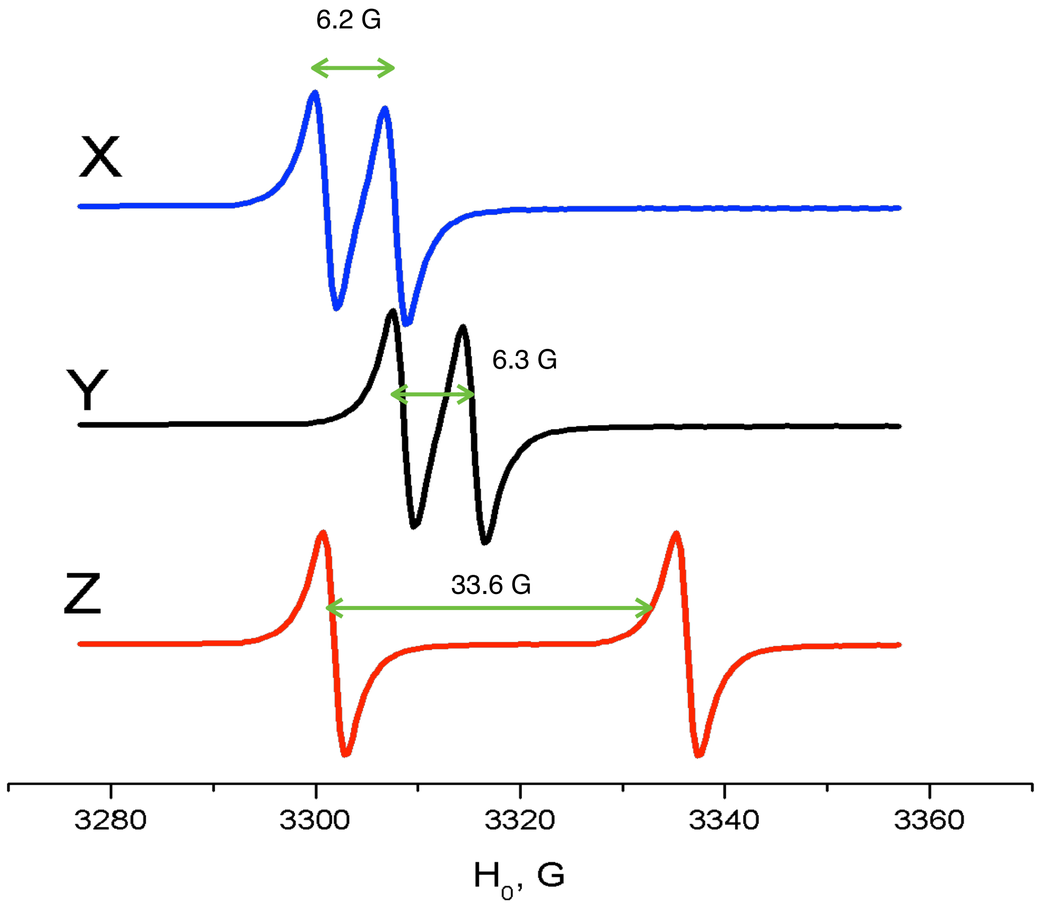

$$H = H^* - \frac{a}{g\beta} m_I$$

$$= \frac{h\nu}{g\beta} - A\, m_I$$

$$= \frac{h\nu}{\beta g(\theta,\phi)} - m_I A(\theta,\phi)$$

g_x=2.0091, g_y=2.0061, g_z=2.0023

I=1, A_x= 6.2, A_y = 6.3, A_z=33.6

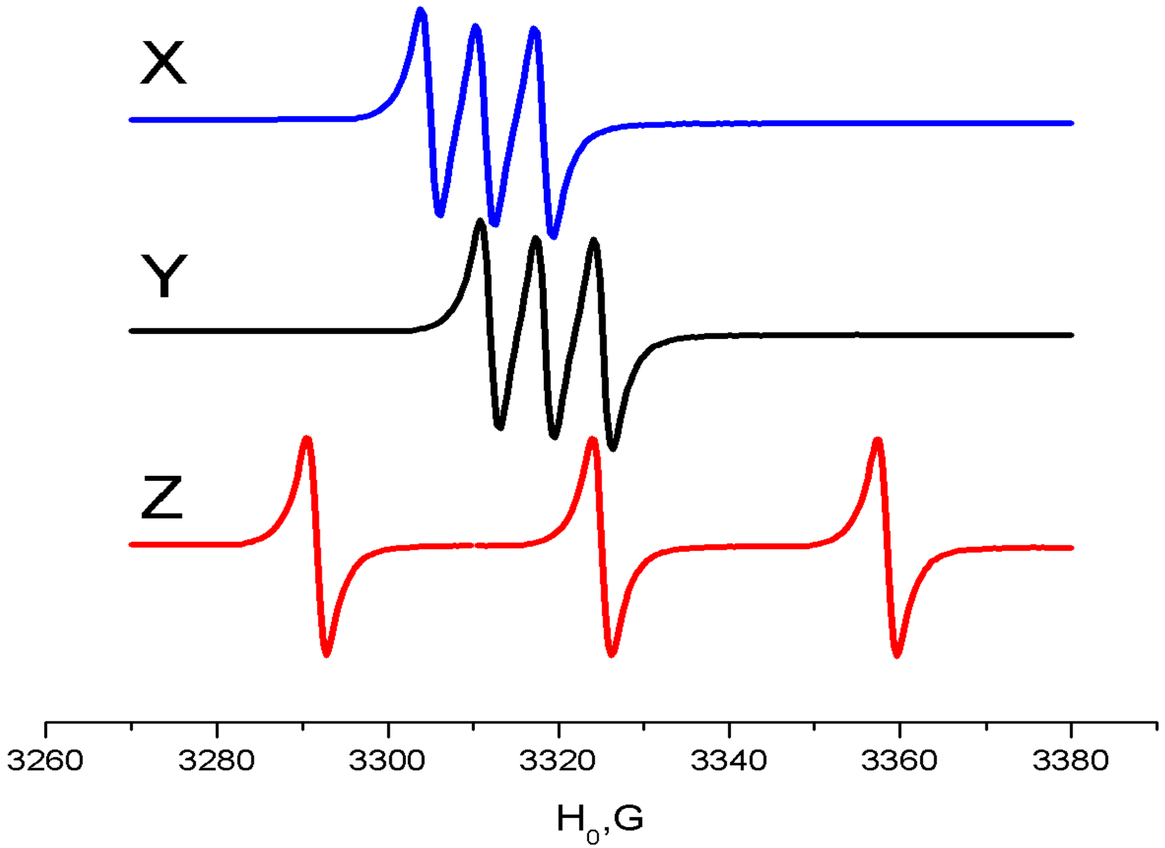

g_x=2.0091, g_y=2.0061, g_z=2.0023

I=1, A_x= 6.2, A_y = 6.3, A_z=33.6

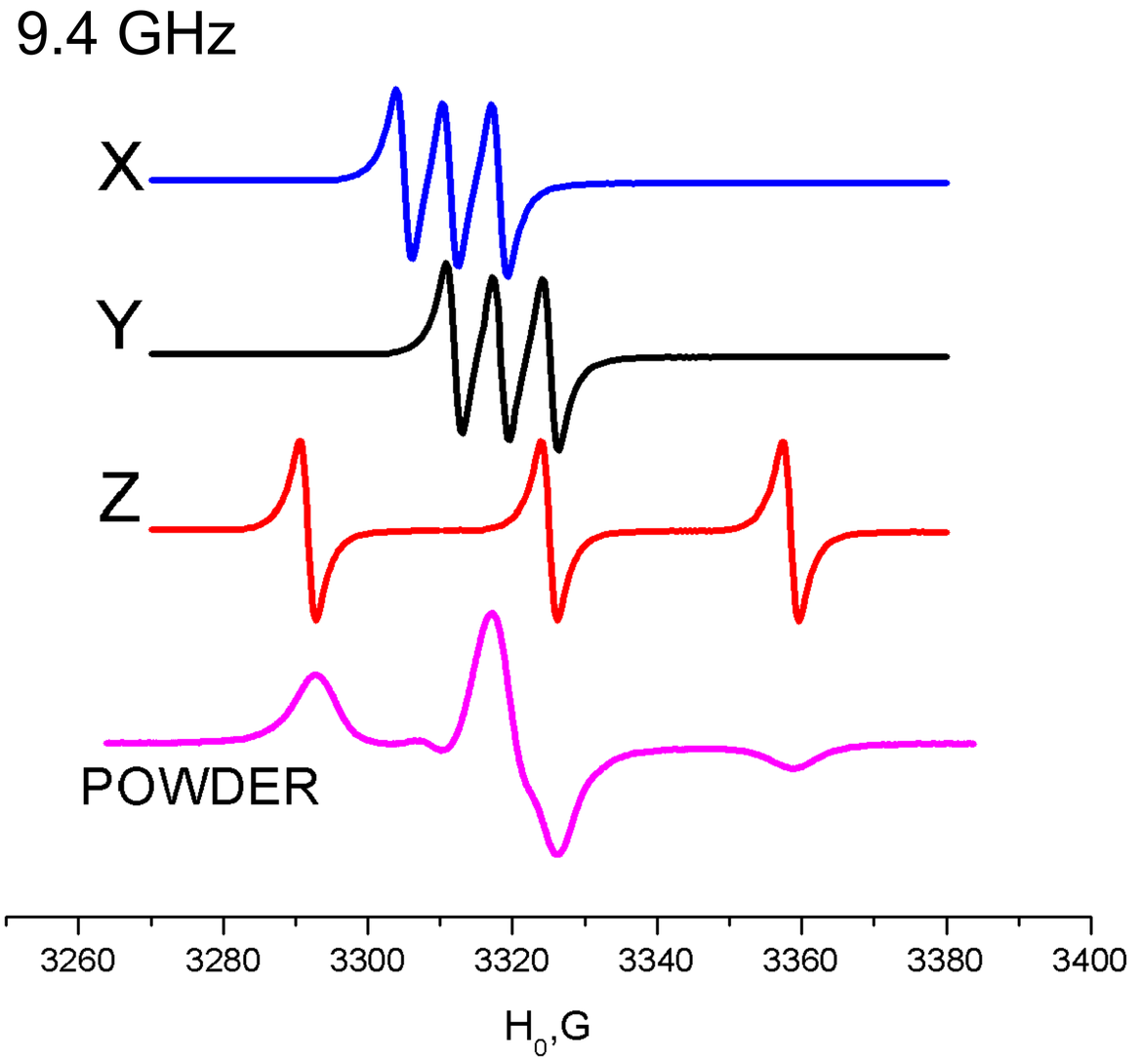

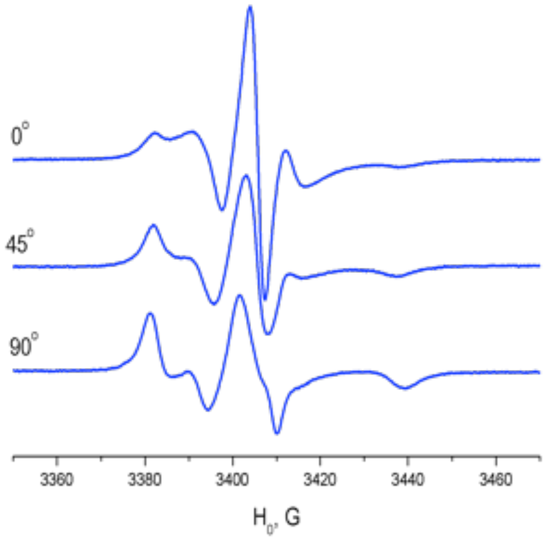

Real data is blurred due to mosaicity

MOMD: microscopic order – macroscopic disorder.
An important case in biology

All orientations of the membrane normal relative to the magnetic field are averaged in vesicles:

g_x=2.0091, g_y=2.0061, g_z=2.0023
I=1, A_x= 6.2, A_y = 6.3, A_z=33.6

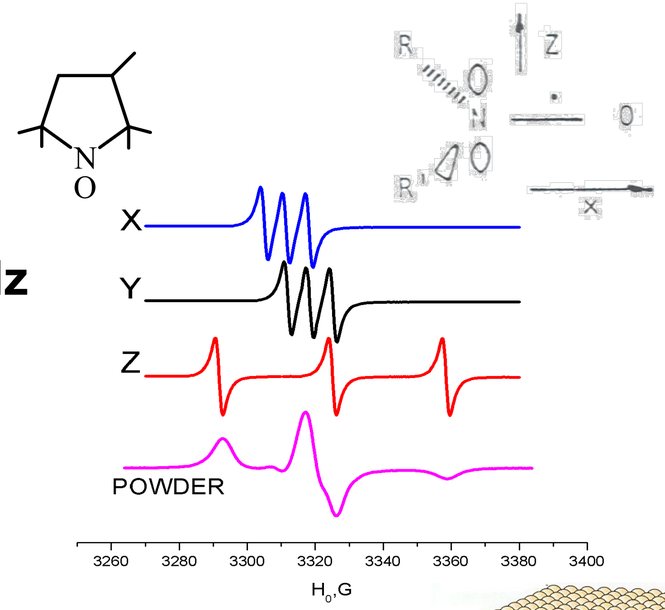

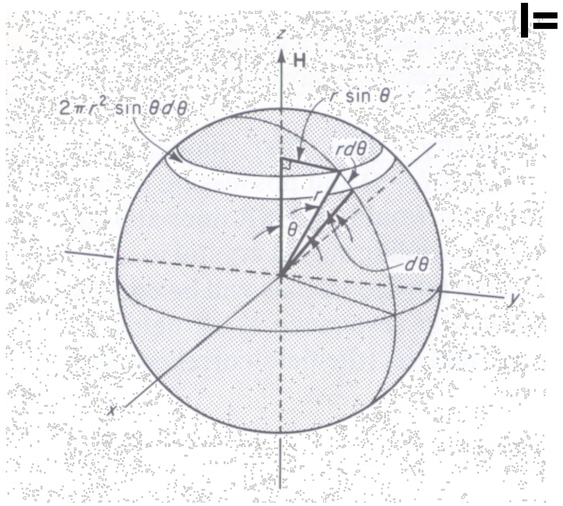

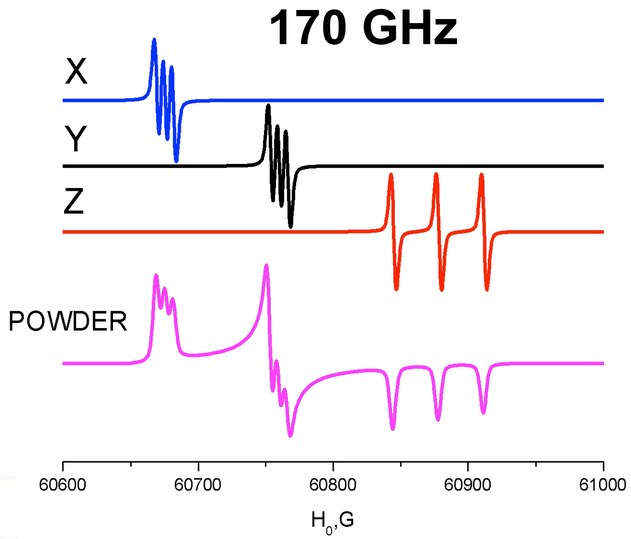

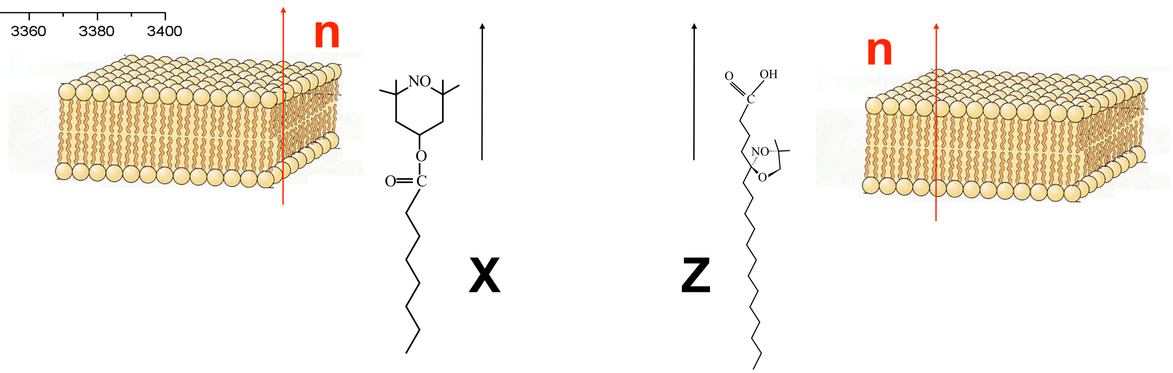

For a macroscopically disordered sample the orientation of the nitroxide moiety manifests itself as a result of anisotropic molecular motion around the principal axis of the molecular frame

Microscopic Ordered and Macroscopic Disorder (MOMD)

e.g. Membrane Vesicles

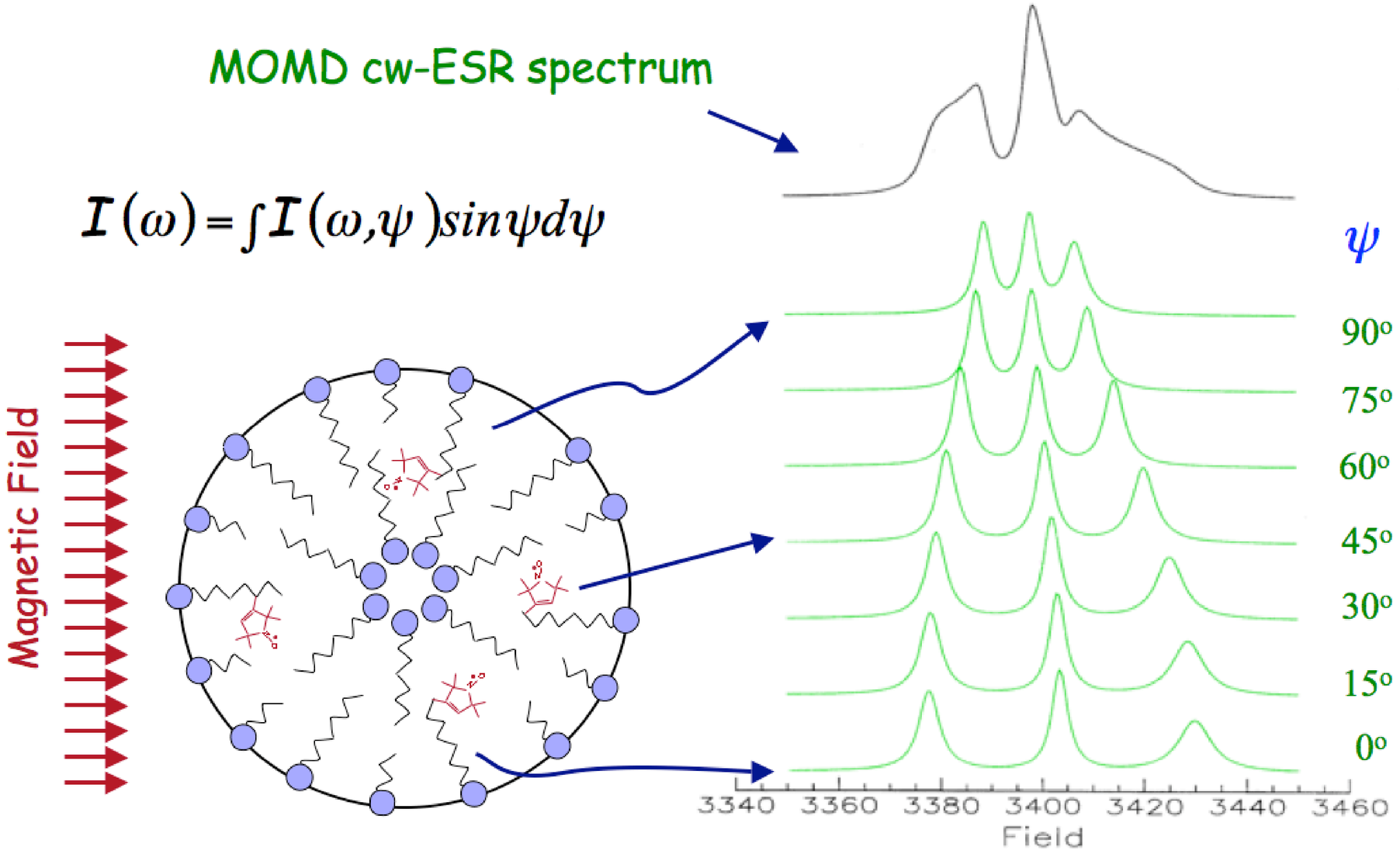

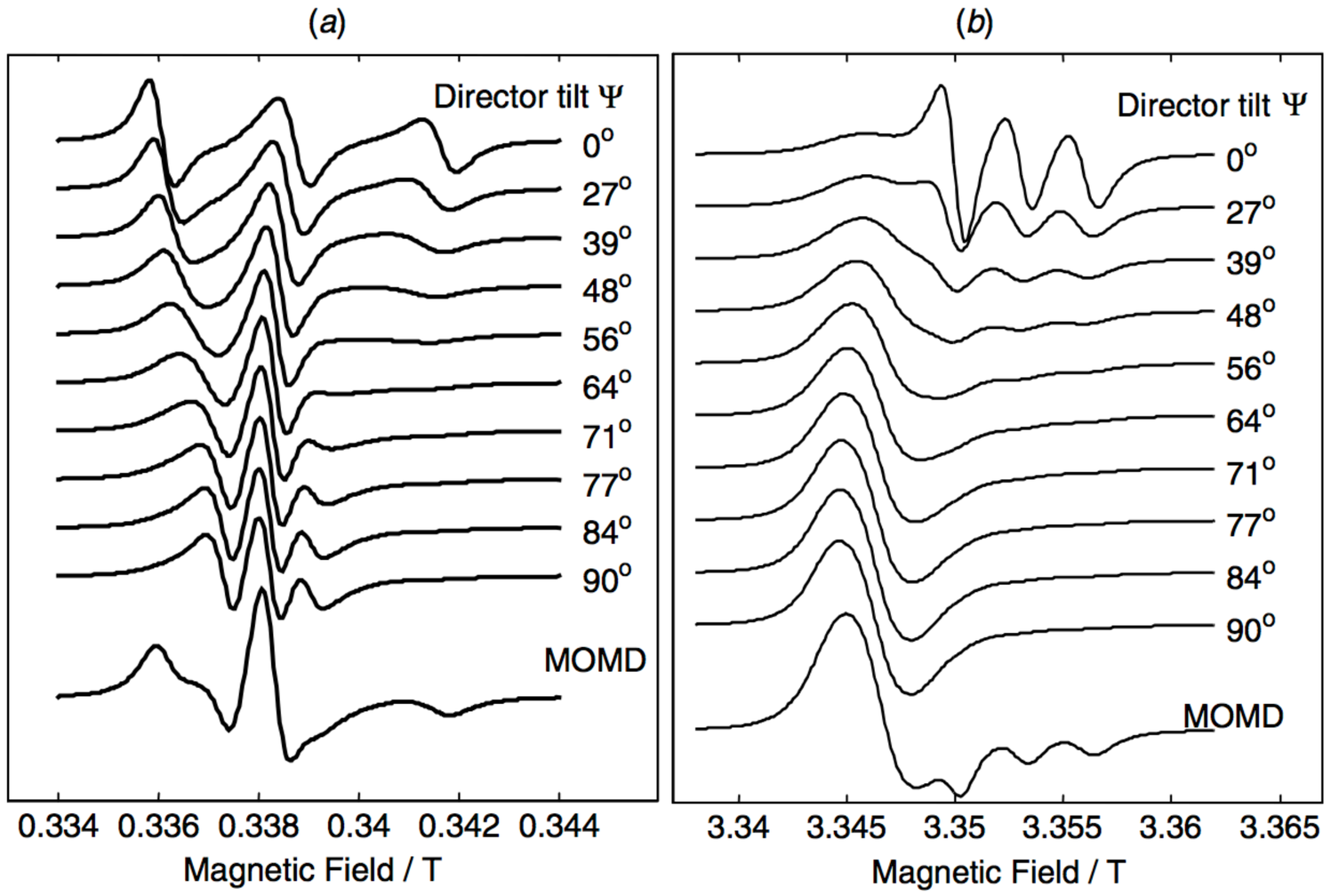

Fig. 12. Components of a MOMD ESR spectrum of a nitroxide spin label, showing the individual spectra from domains with different tilt angles, and integrated MOMD spectrum at the bottom, for 9 GHz (left-hand side) and 94 GHz (right-hand side).

High field EPR spectroscopy is the ***g-resolved spectroscopy***, the regions corresponding different orientations of the magnetic axis relative to the external magnetic field

do not overlap

$$H = H^* - \frac{a}{g\beta} m_I$$

$$= \frac{h\nu}{g\beta} - A\, m_I$$

$$= \frac{h\nu}{\beta g(\theta,\phi)} - m_I A(\theta,\phi)$$

$$H = \frac{h\upsilon}{g\beta}$$

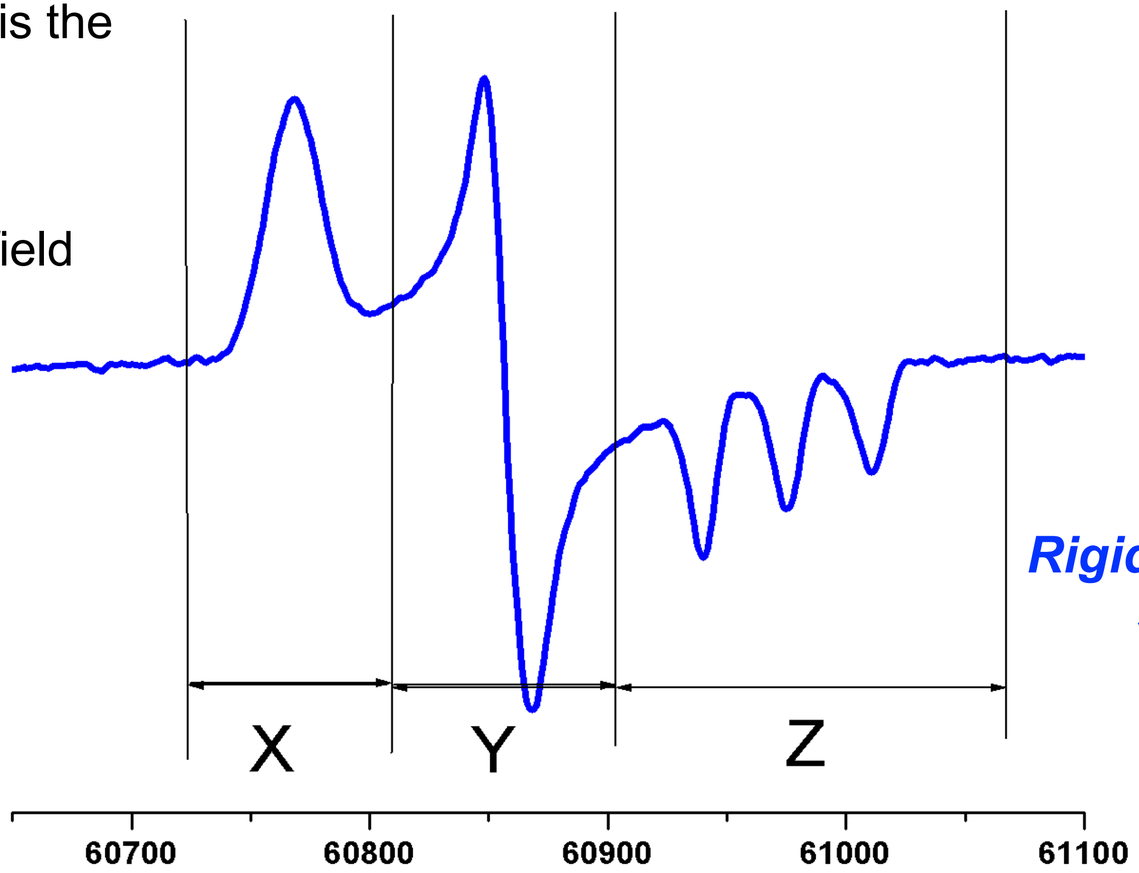

Rigid-limit (frozen) spectrum

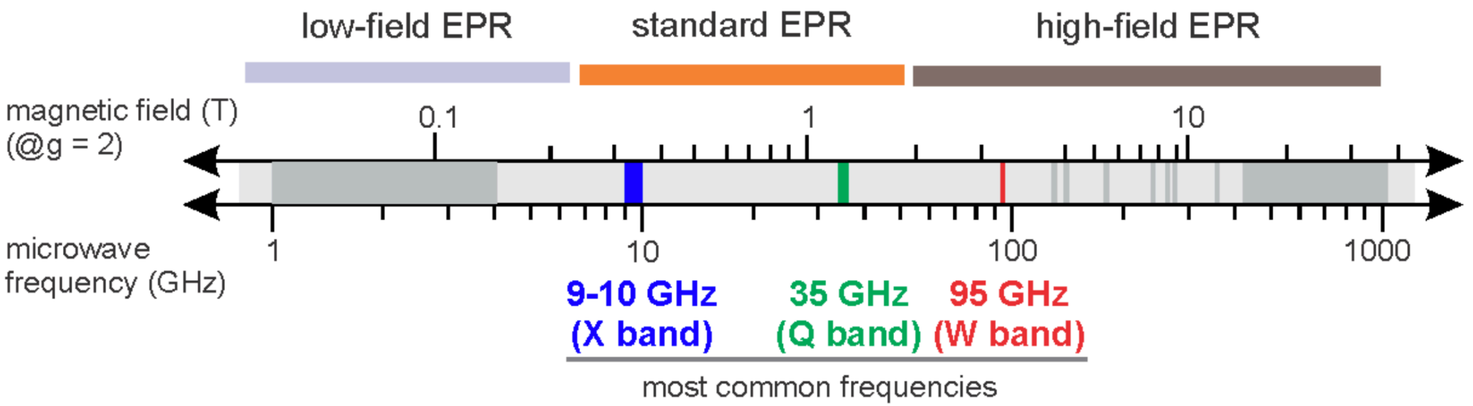

g_x=2.0091, g_y=2.0061, g_z=2.0023

I=1, A_x= 6.2, A_y = 6.3, A_z=33.6

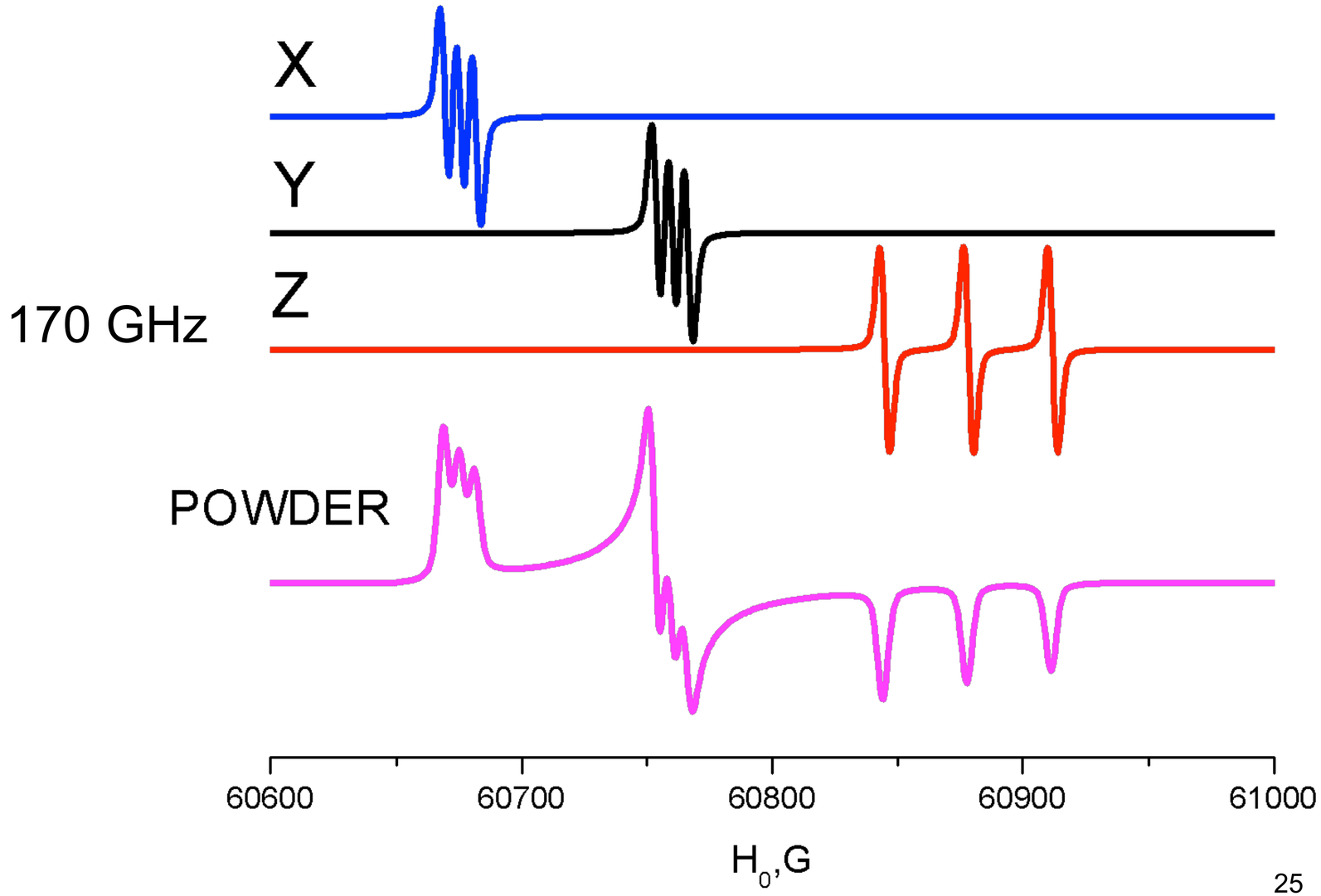

(a) X-band Spectrum

Dominated by HF-term

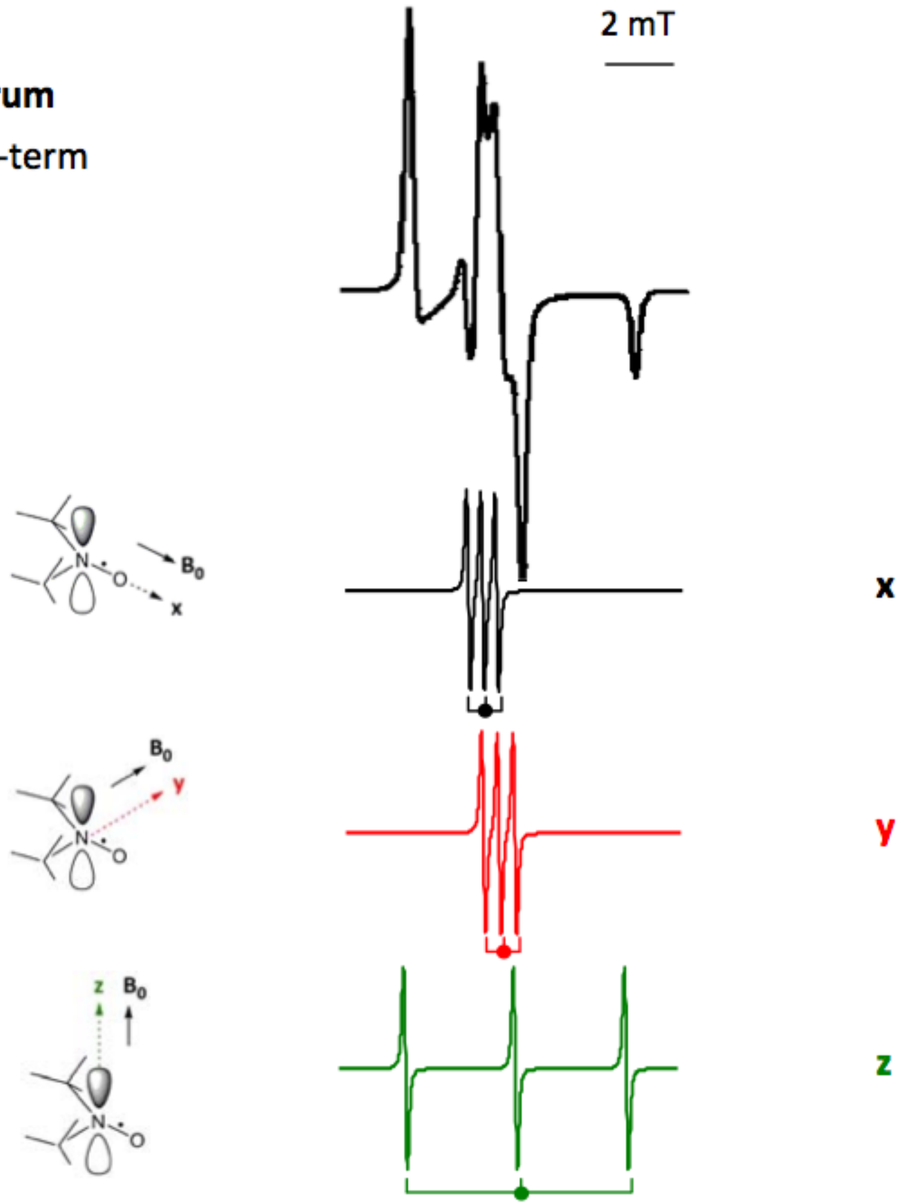

(b) W-band Spectrum

Dominated by EZ-term

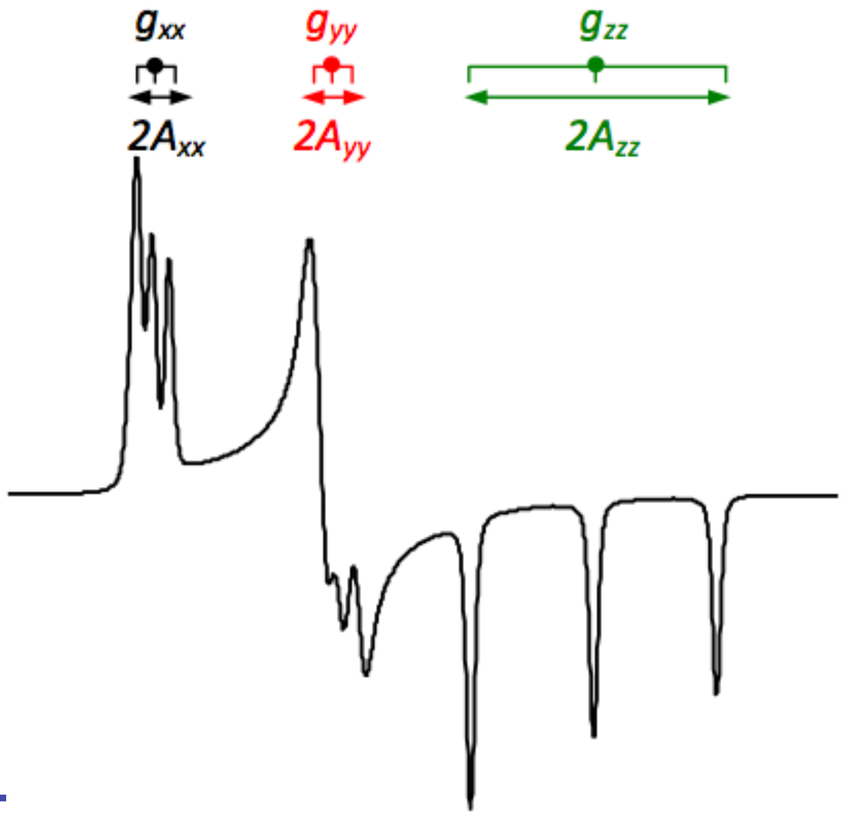

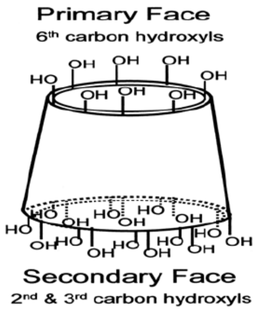

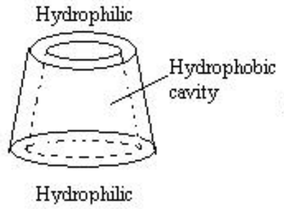

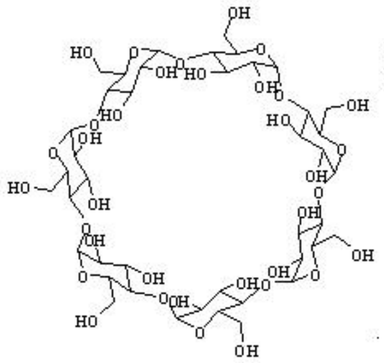

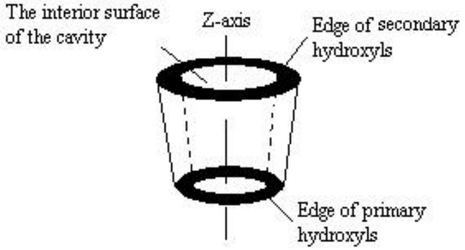

Cyclodextrins (CDs) are cyclic oligomers of D-glucopyranose. Due to the presence of a hydrophobic cavity in the molecule they are able to form guest–host complexes with a variety of organic compounds.

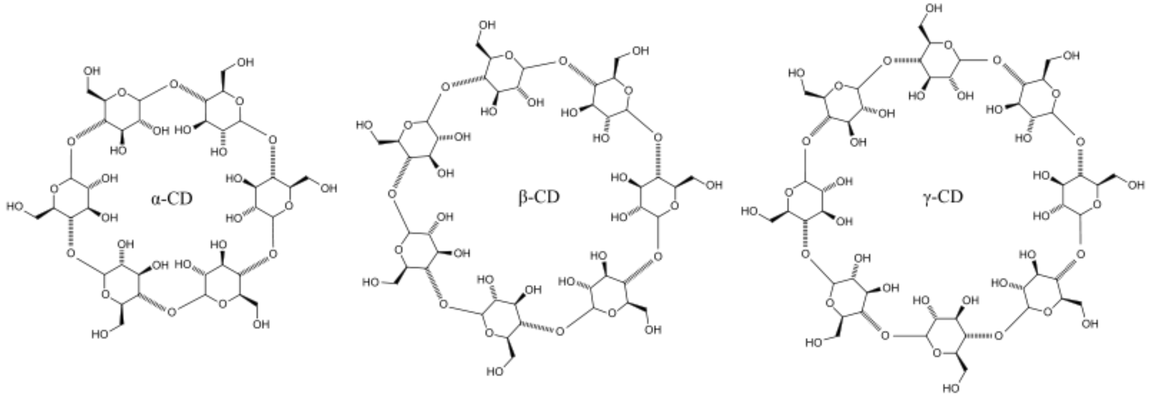

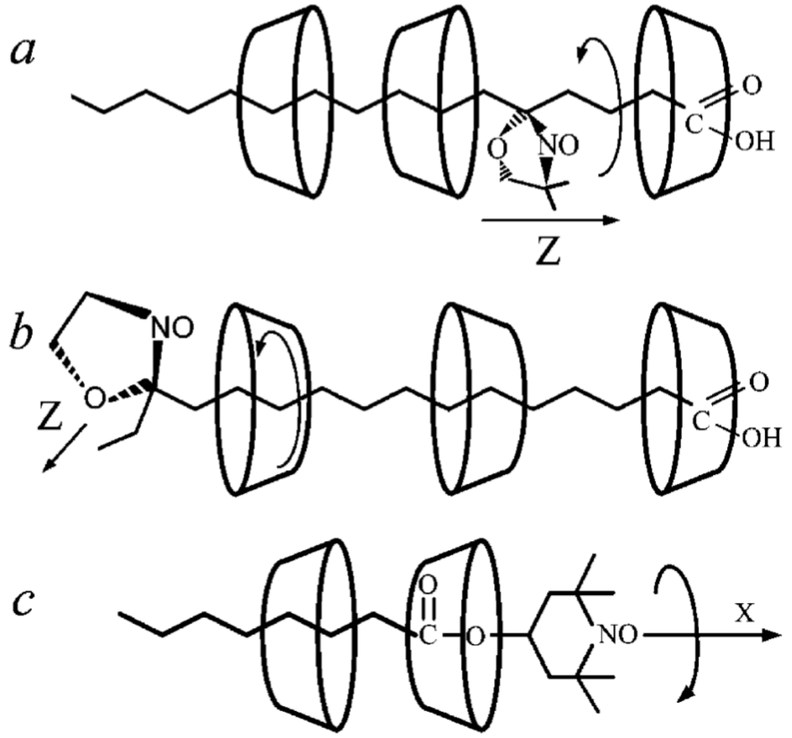

Fig. 7 Schematic drawing of the hypothetical arrangement of cyclodextrin molecules around spin-labeled compound: (a) 5-sasl (b) 16-sasl (c) TEMPOyl-caprylate.

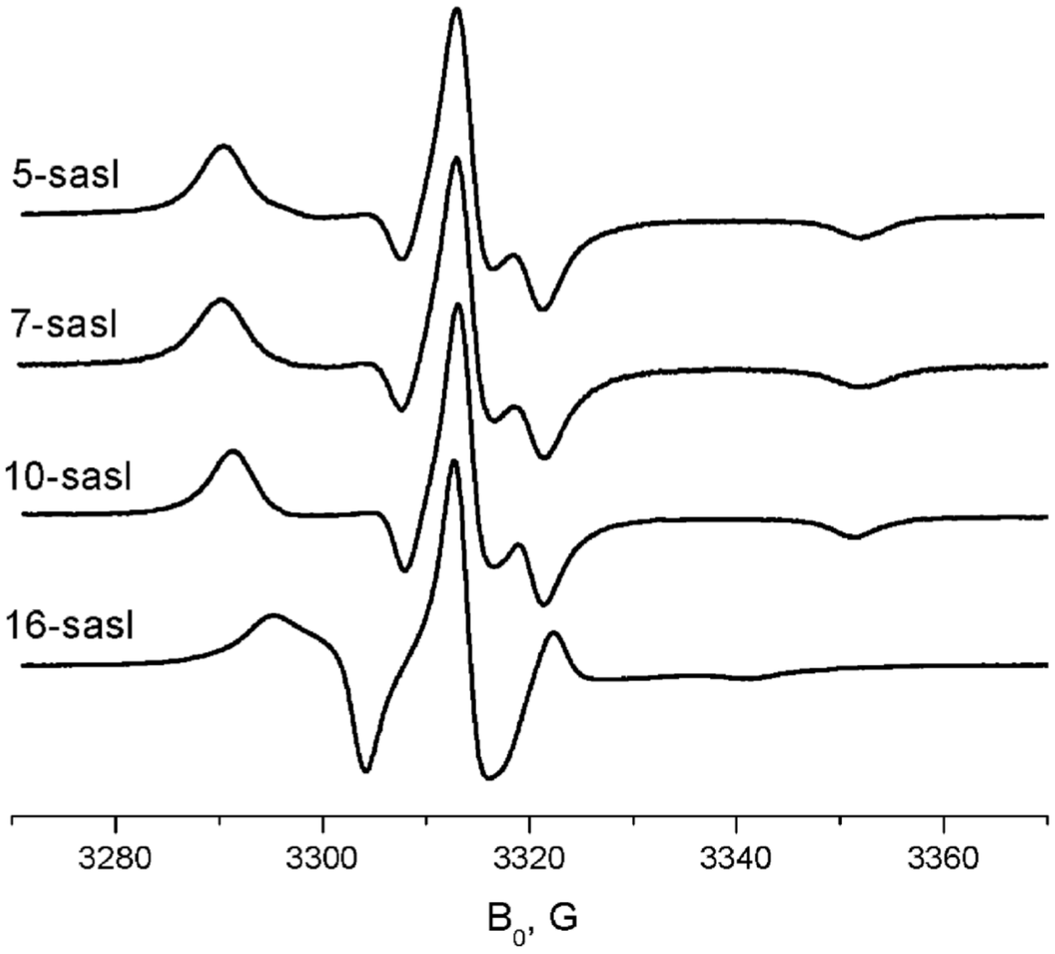

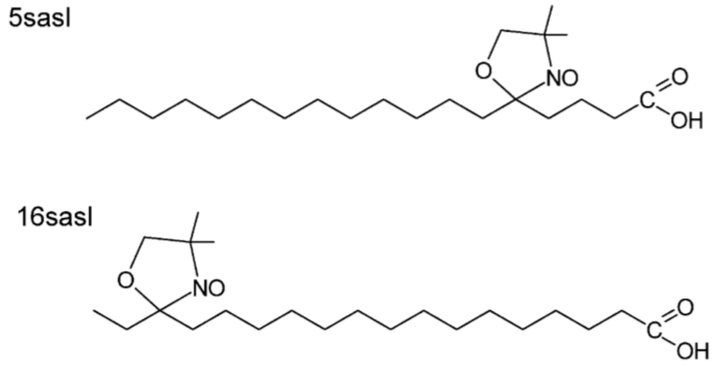

- **Slow-motional spectra, rigid-limit like at room T. (except 16-sasl)**
- **Less lineshape change at 9 GHz ==> less dynamical information.**
- **Sample condition: solid like with some crystallohydrate water.**

Fig. 4 9 GHz spectra of 5-, 7-, 10- and 16-doxyl stearic acids at 293 K in solid γ-CD.

HFHF ESR provides better orientational resolution.

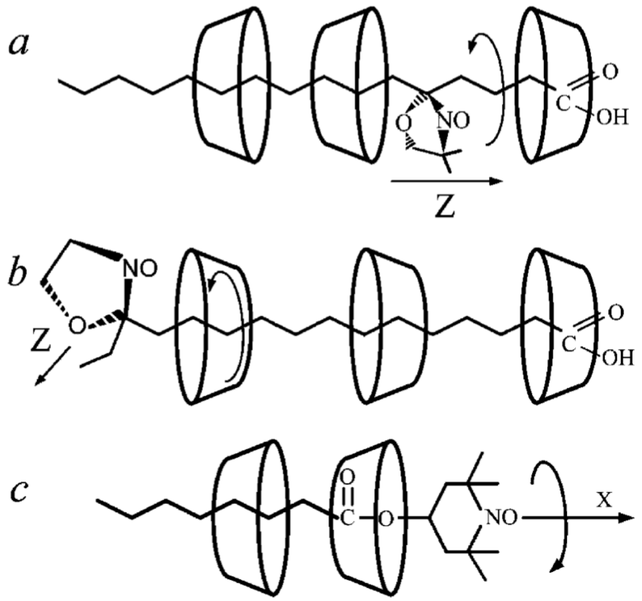

Fig. 7 Schematic drawing of the hypothetical arrangement of cyclodextrin molecules around spin-labeled compound: (a) 5-sasl (b) 16-sasl (c) TEMPOyl-caprylate.

240 GHz, 5-sasl in γ-CD

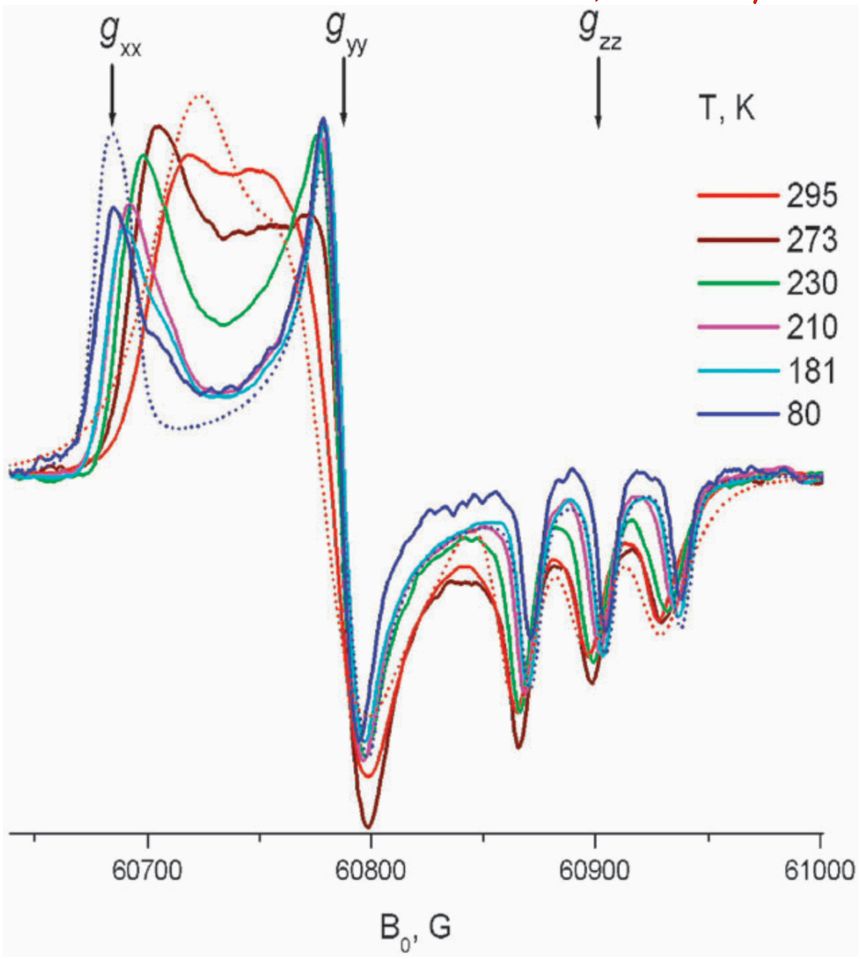

Fig. 5 170 GHz spectra of 5-sasl in solid γ-CD at 80–295 K. Dotted lines show simulations for 80 K (rigid limit) and 295 K.

As a result, once motional effects are discernable in the spectrum, one can discern about which axis (or axes) the motion occurs.

At low T it enables the unambiguous determination of the A and the g tensors.

At high T but in solid state (not tumbling motions), local enhanced rotation improves the spectral resolution; low-field region is blurred by the motion-induced ambiguity effect.

HFHF ESR provides better orientational resolution.

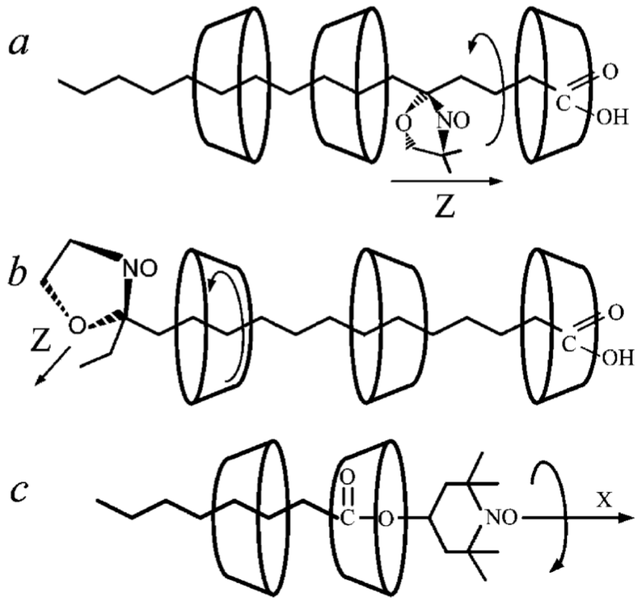

Fig. 7 Schematic drawing of the hypothetical arrangement of cyclodextrin molecules around spin-labeled compound: (a) 5-sasl (b) 16-sasl (c) TEMPOyl-caprylate.

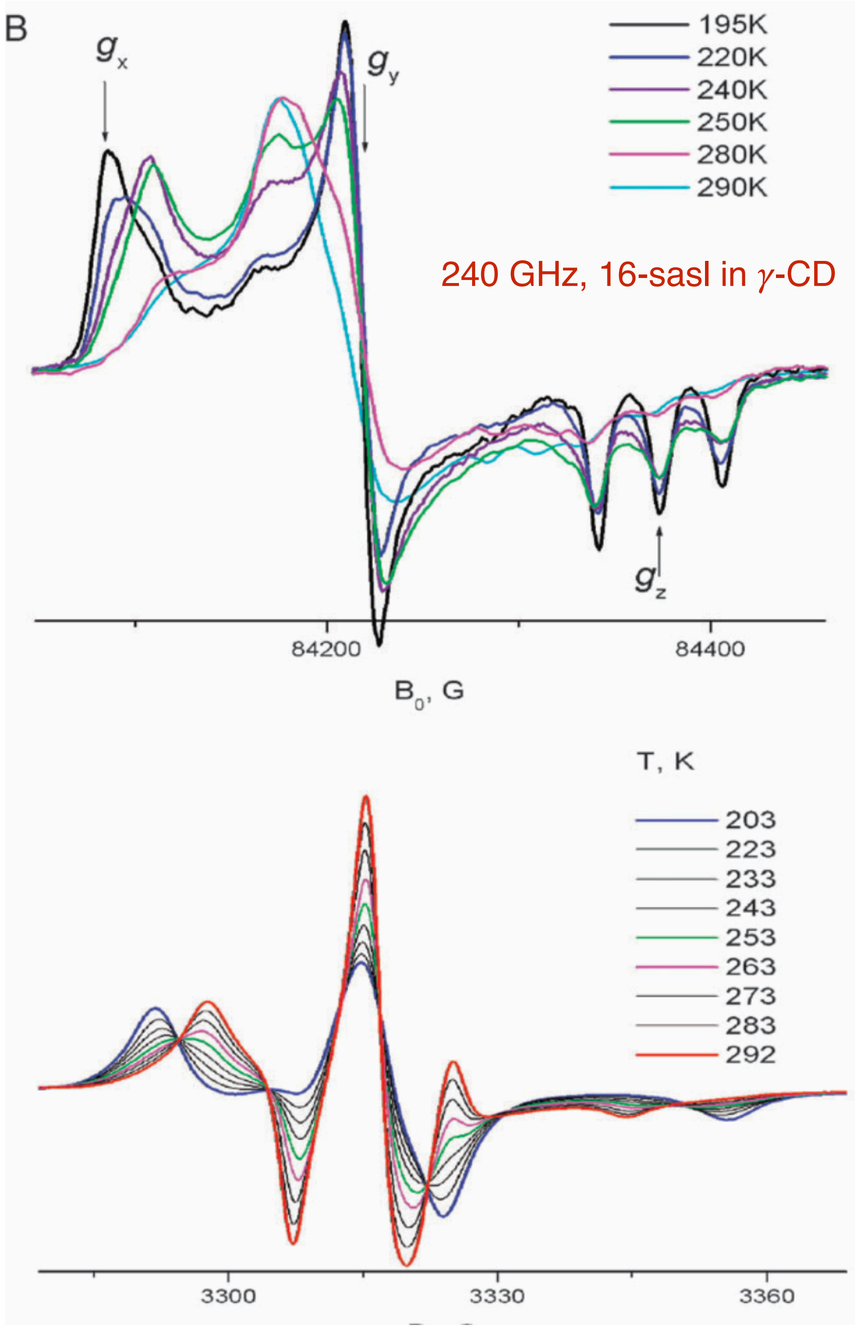

As a result, once motional effects are discernable in the spectrum, one can discern about which axis (or axes) the motion occurs.

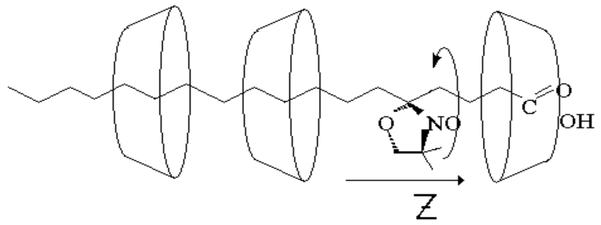

Z-rotation vs. slow motion

5 sasl wet
5 sasl pumped

9.4 GHz

170 GHz

Averaging *effective* tensor components

$(g_{xx}+ g_{yy})/2, (g_{xx}+ g_{yy})/2, g_{zz}$

$(A_{xx}+ A_{yy})/2, (A_{xx}+ A_{yy})/2\ A_{zz}$

Averaging real tensor components

$g_{xx}, g_{yy}, g_{zz}, A_{xx}, A_{yy}, A_{zz}$

3040 3060 3080 3100 3120 3140 3160 3180

Room T

60600 60700 60800 60900 61000 61100 61200

HFHF ESR allowed us to demonstrate Z- and X-axial rotation and determine the relevant rotational diffusion constants and potential barriers. Such determination at 9 GHz is either impossible (Z-rotation) or inaccurate (X-rotation).

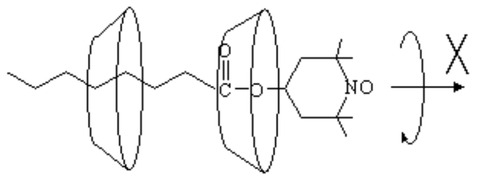

X-rotation

Averaging *effective* tensor components

g_{xx}, $(g_{yy}+ g_{zz})/2$, $(g_{yy}+ g_{zz})/2$,

A_{xx}, $(A_{yy}+ A_{zz})/2$, $(A_{yy}+ A_{zz})/2$

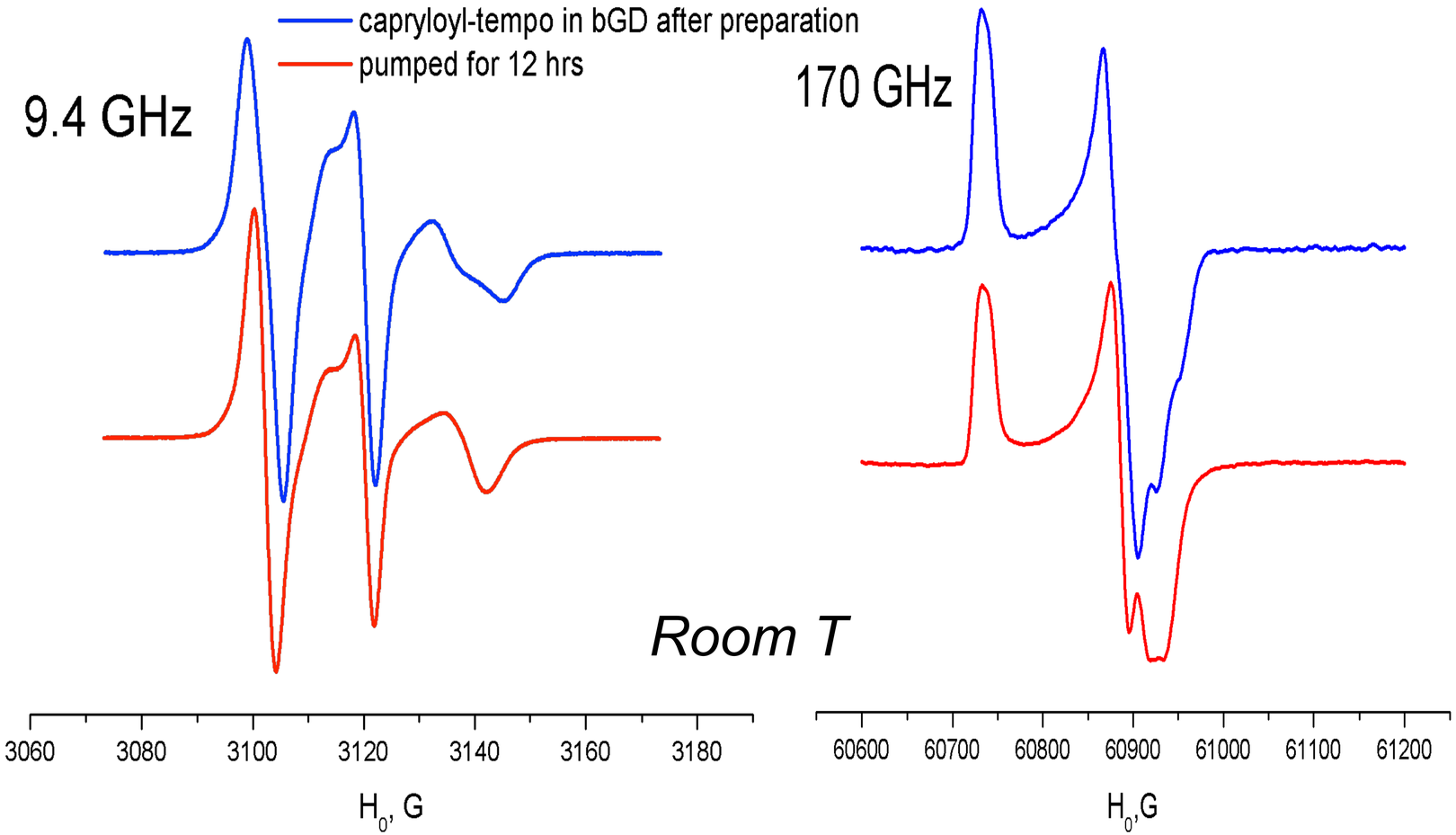

Diffusion tilt angle

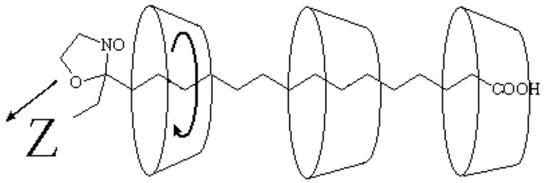

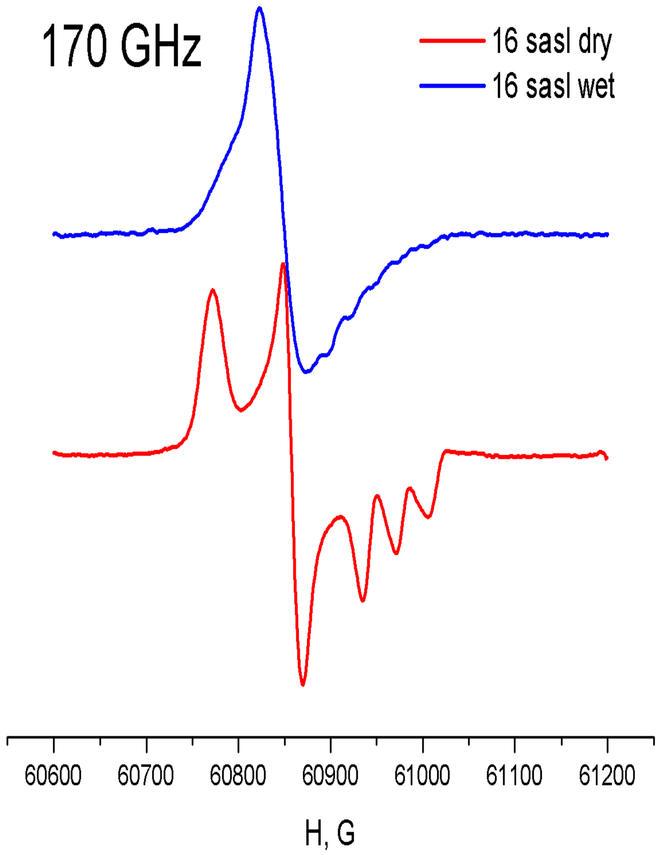

Y-rotation

Averaging *effective* tensor components

$(g_{xx}+ g_{zz})/2$, g_{yy}, $(g_{xx}+ g_{zz})/2$,
$(A_{xx}+ A_{zz})/2$, A_{yy}, $(A_{xx}+ A_{zz})/2$

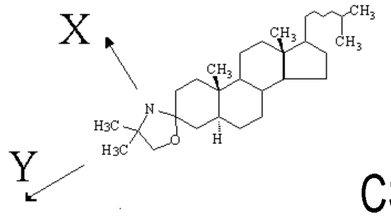

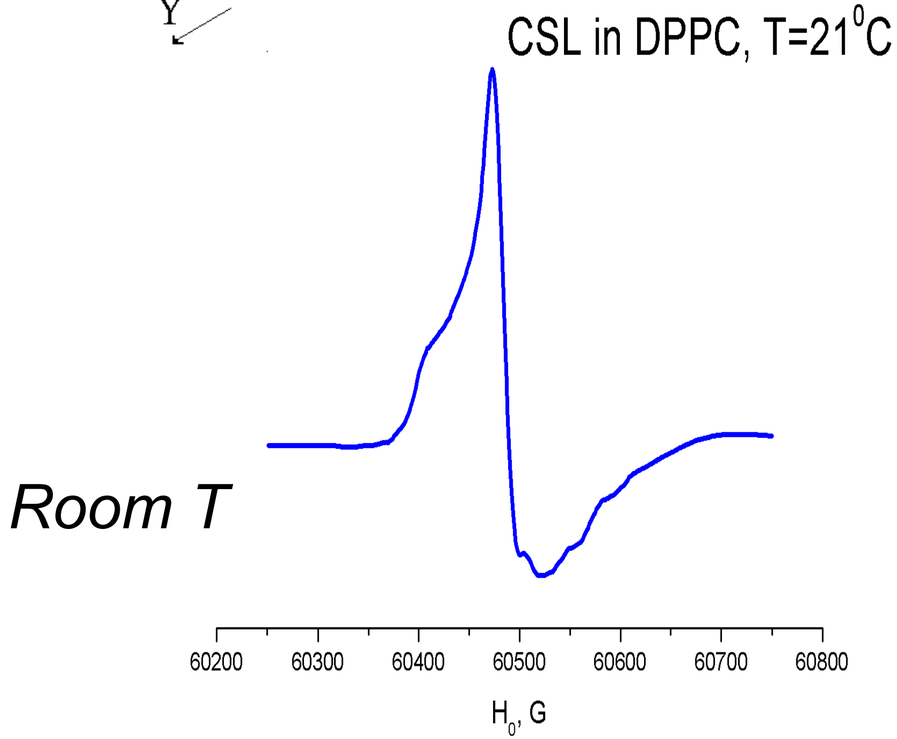

Room T

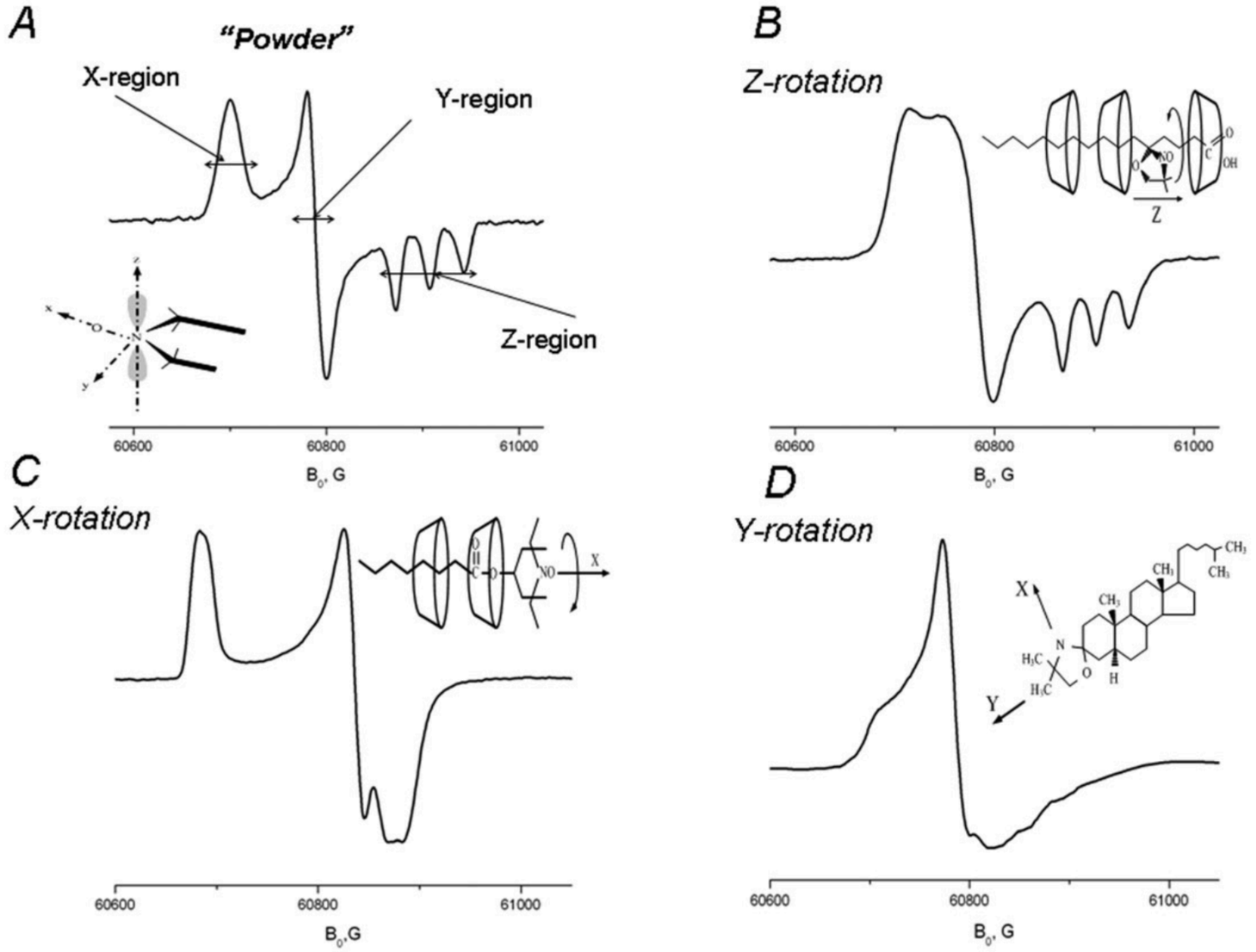

Fig. 3 170 GHz spectra of nitroxide radicals corresponding to different modes of molecular motion: (A) 5-sasl in γ-CD with crystallohydrate water removed by overnight evacuation at 293 K: rigid limit spectrum. (B) 5-sasl in γ-CD crystallohydrate at 292 K. (C) TEMPOyl-caprylate in β-CD at 293 K. (D) CSL spin label in the DPPC membrane at 295 K. Insert A shows the principal magnetic axes of the nitroxide group. Inserts B–D show the corresponding mode of molecular motion.

X-rotation

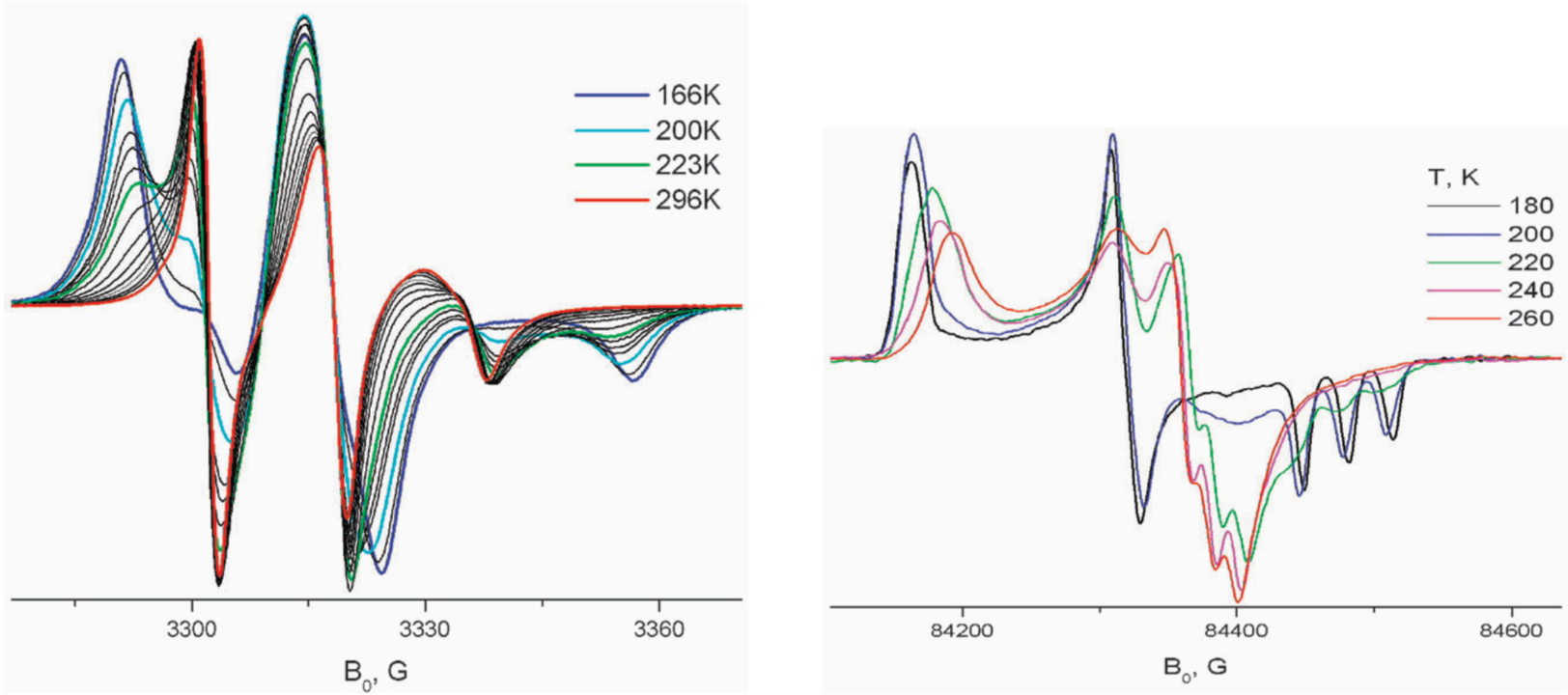

Fig. 15 TEMPOyl caprylate in γ-CD. Temperature dependence at 240 GHz (upper image) and 9 GHz (lower image).

*Dynamics **vs.** Dynamics + Orientational resolution*

ESR on aligned membranes

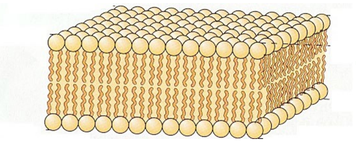

Spin-labeled gramicidin A in DPPC, 22⁰ C

Aligned membrane

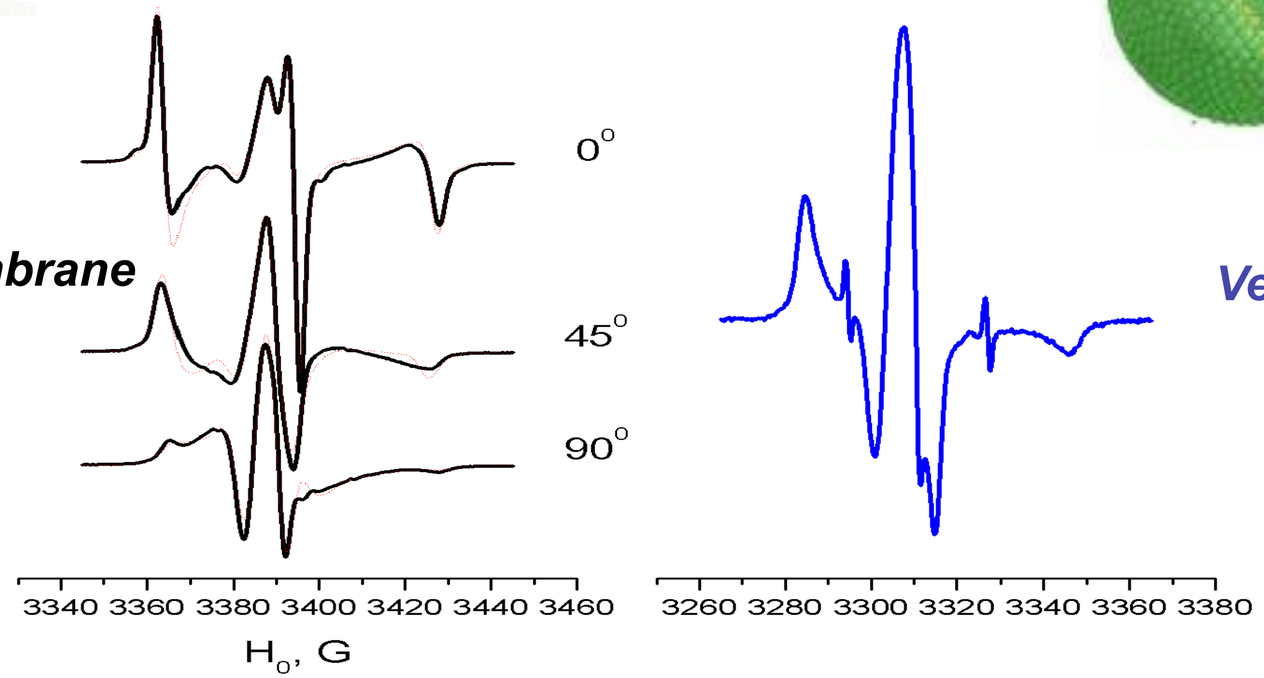

Vesicles

Simulation of angular dependent spectra is much freer of ambiguity, compared to vesicles

Application of aligned membranes allows extracting information on relative orientation of diffusion and magnetic axes, which can not be obtained from vesicles

Microtome technique on aligned membranes

High frequency ESR *requires very thin (<100 mm) flat samples with* B_0 *directed perpendicular to the sample in order to minimize dielectric losses*

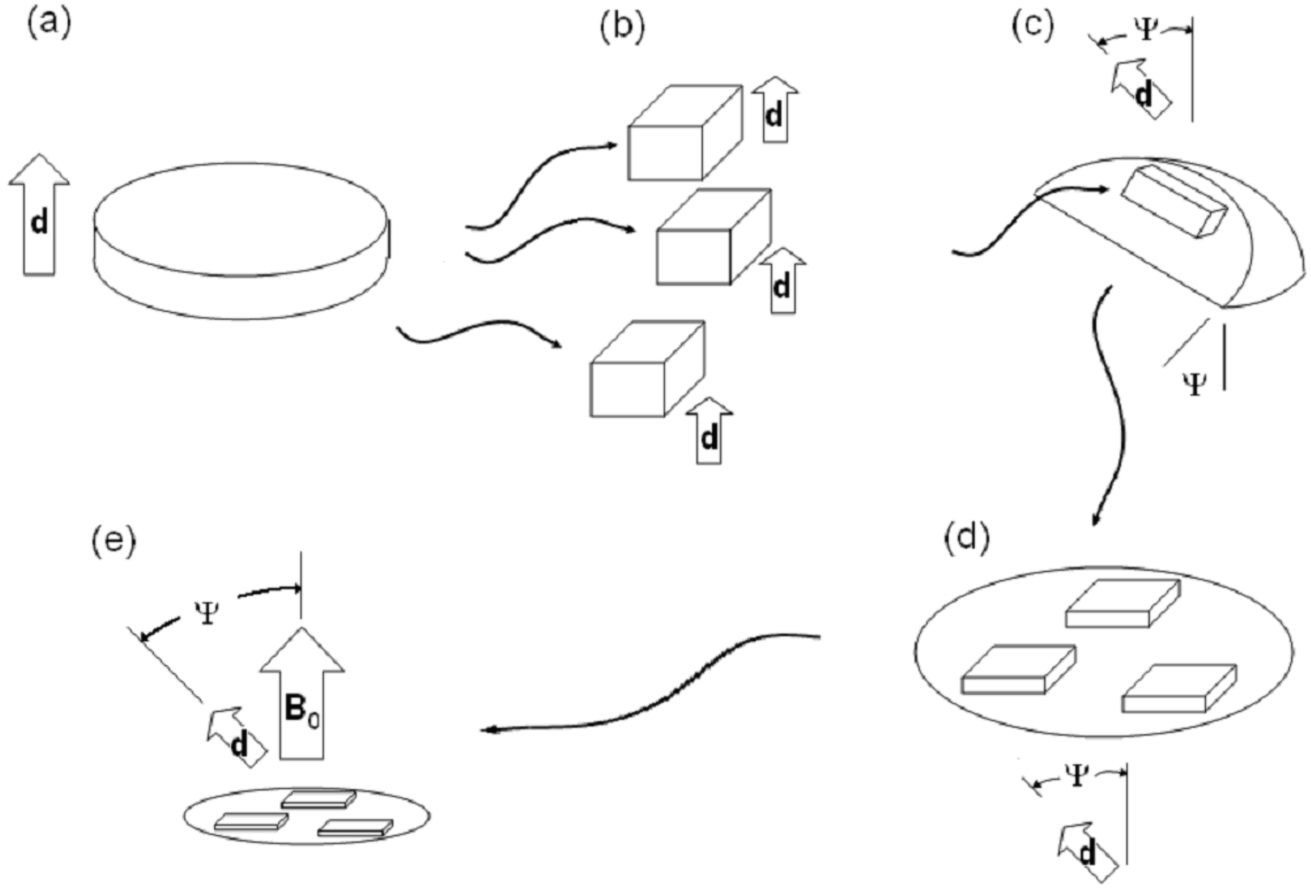

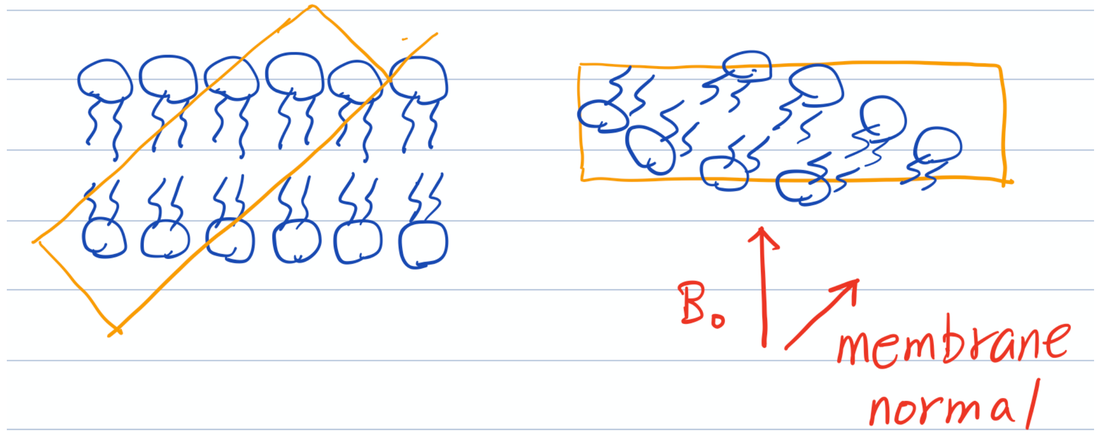

High-field ESR on aligned membranes

in different orientation of the membrane normal relative to B_o

ISDU aligned DPPC membrane sample is 300 micrometer think

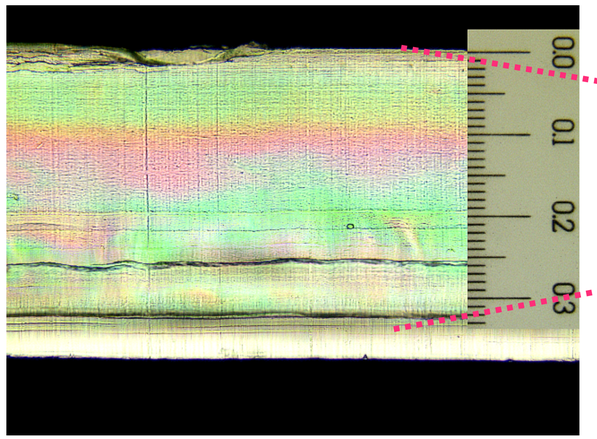

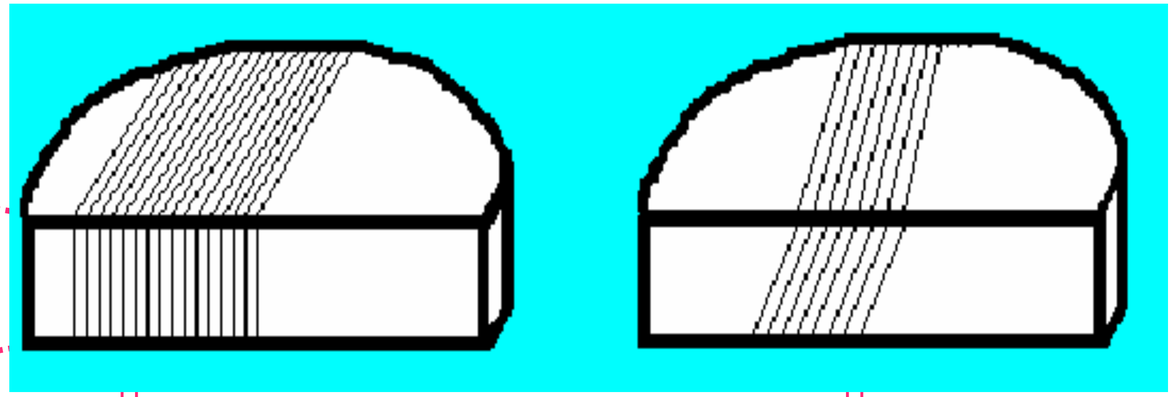

80micrometer slices cut of the sample

are utilized in high-field ESR

Spin labeled Gramicidin A in DPPC at 170 GHz

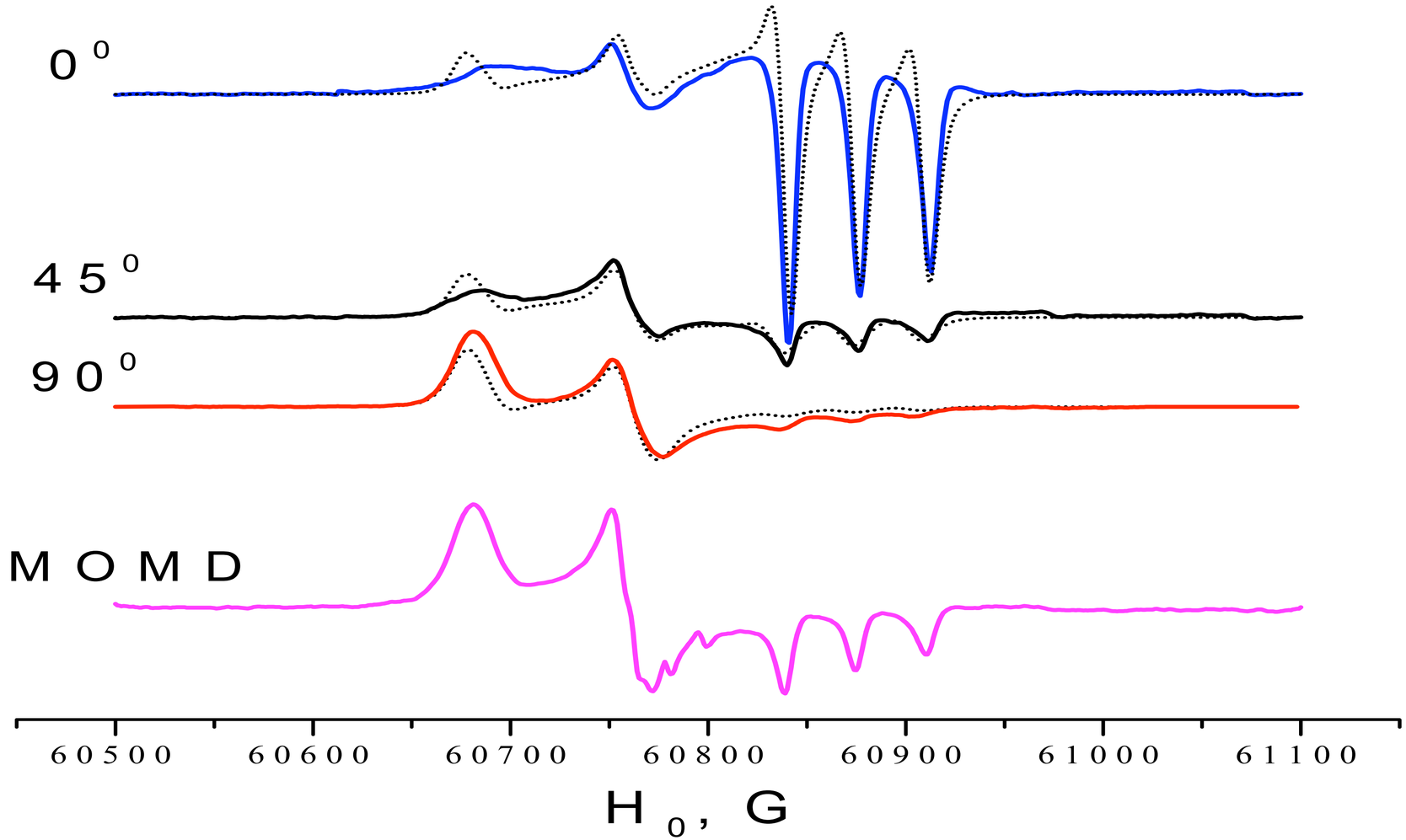

Spin-labeled Gramicidin A in Oriented Membrane (DPPC)

- *Slow motional nitroxyl spectrum at 7°C.*
- *Orientation selection at 95 GHz (3.2 mm)*
- *g_z parallel to membrane normal (z-ordered)*

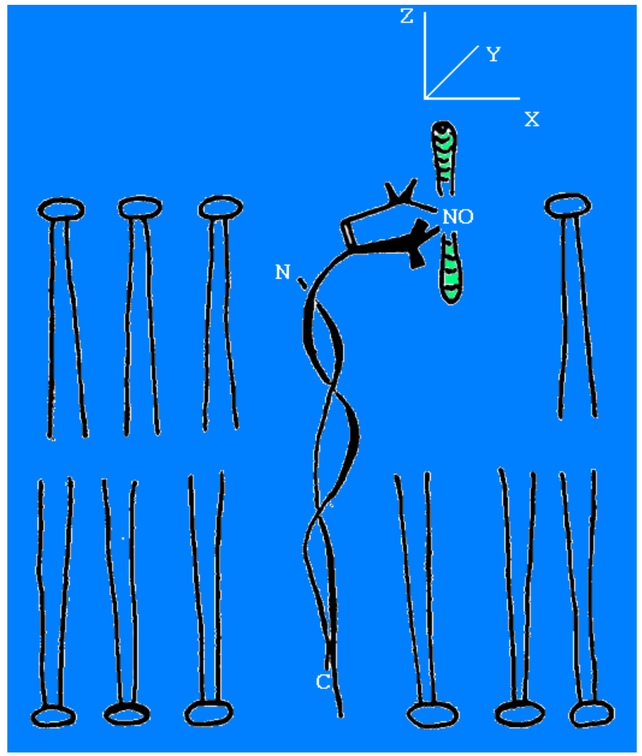

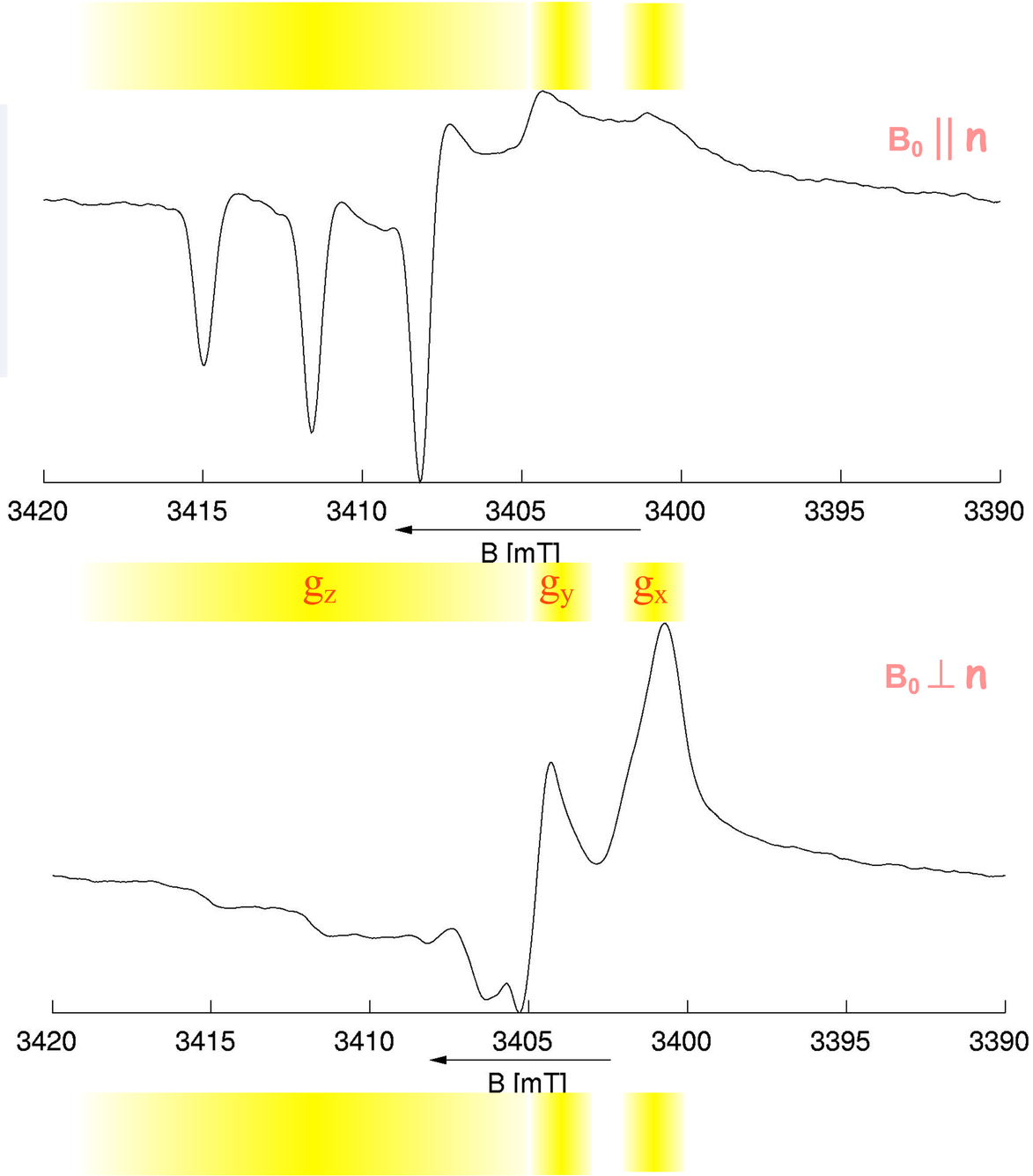

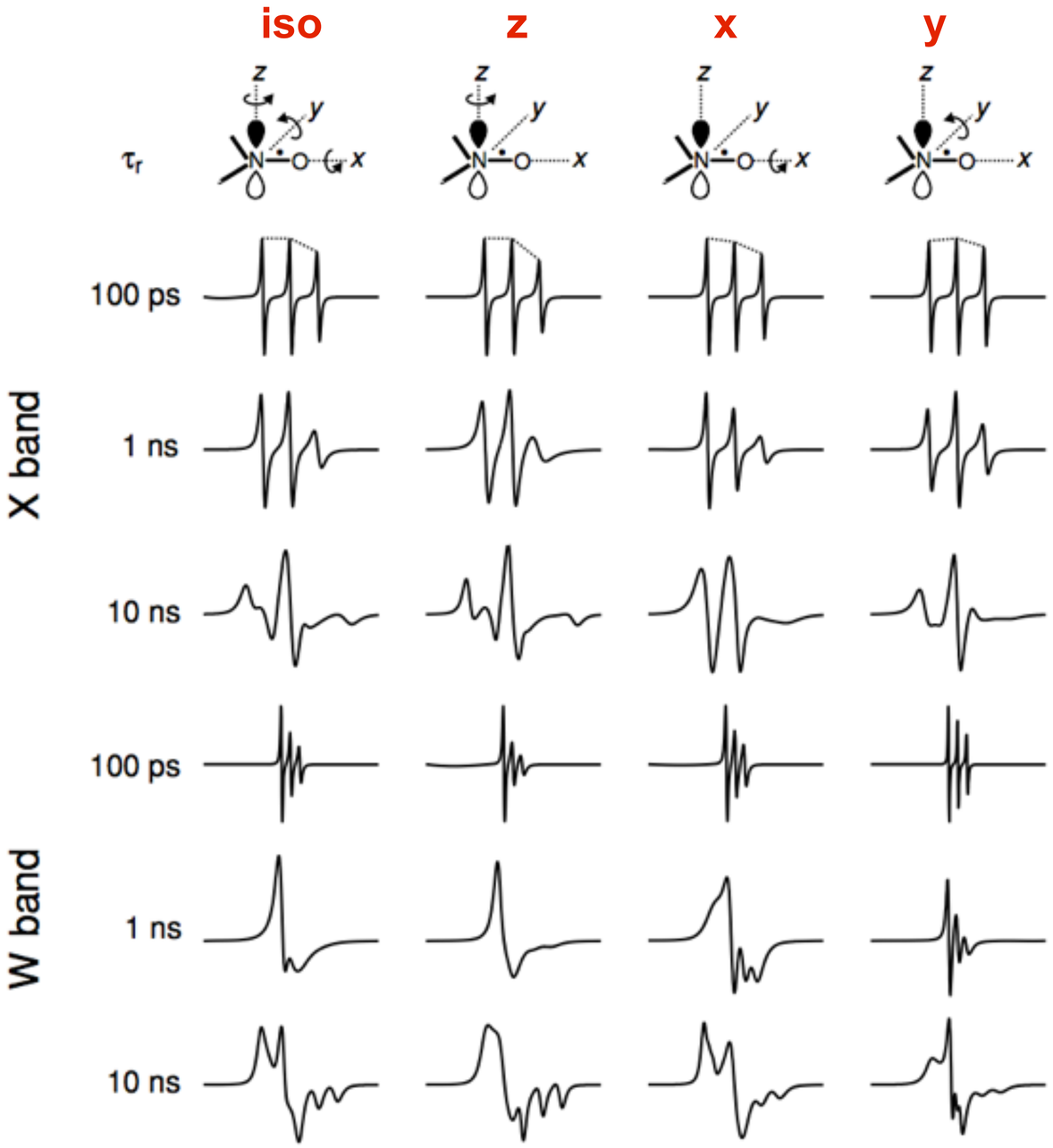

Fig. 1. Dependency of nitroxide spin probe spectra on rotational correlation time, preferential rotation axis, and EPR frequency. Panels from left to right correspond to isotropic rotational diffusion, and preferential rotation about the z, x, and y axis, respectively. Rotational diffusion about the preferred axis is assumed to be ten times faster than about other axes. X-band spectra are centered at 334.8 mT and are 10 mT wide, W-band spectra are centered at 3355 mT and are 30 mT wide. Simulations were performed with the Schneider/Freed suite of programs [21].

Lineshape depends on
1) diffusional rates (dynamics) 2) anisotropic rotations

Nano-confinement Enhances Anisotropic Rotational Dynamics ?

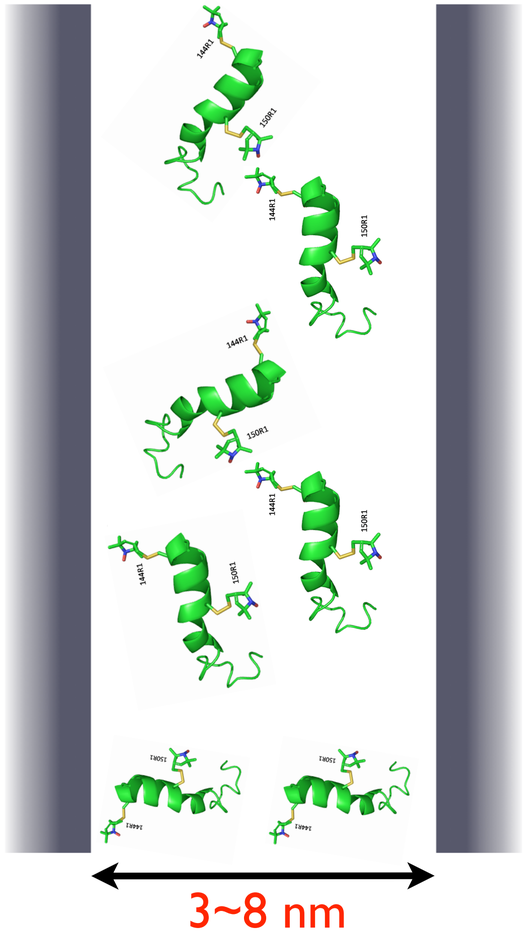

vs.

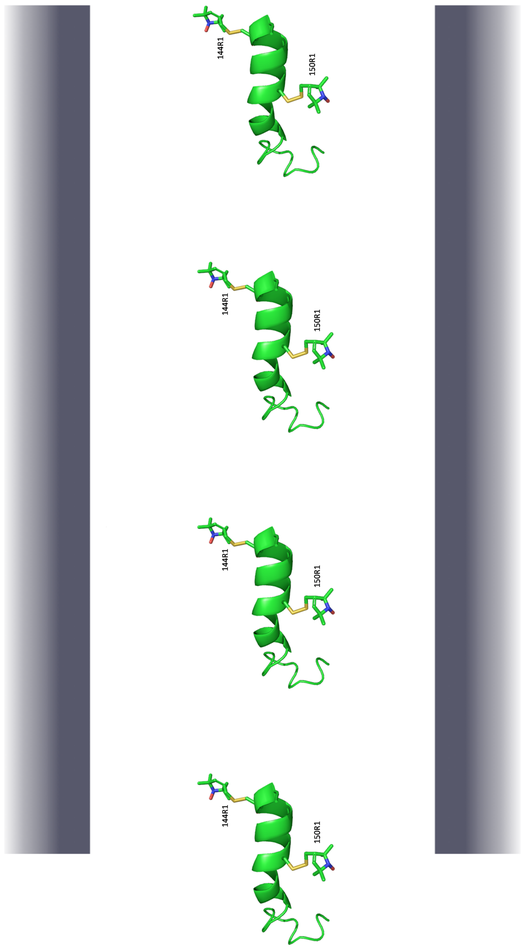

Is ESR useful for probing dynamics of a nanodevice confined deeply within nanostructures?

Peptide Retains its Structure in Nanochannels

PP-3R1 CPPPCPPPPPPPPC

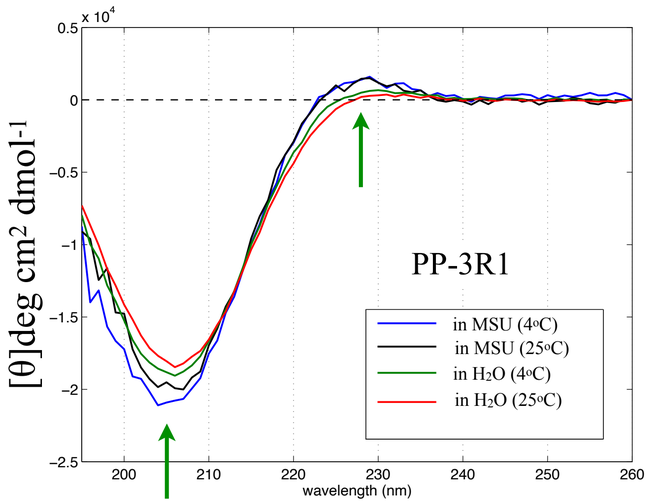

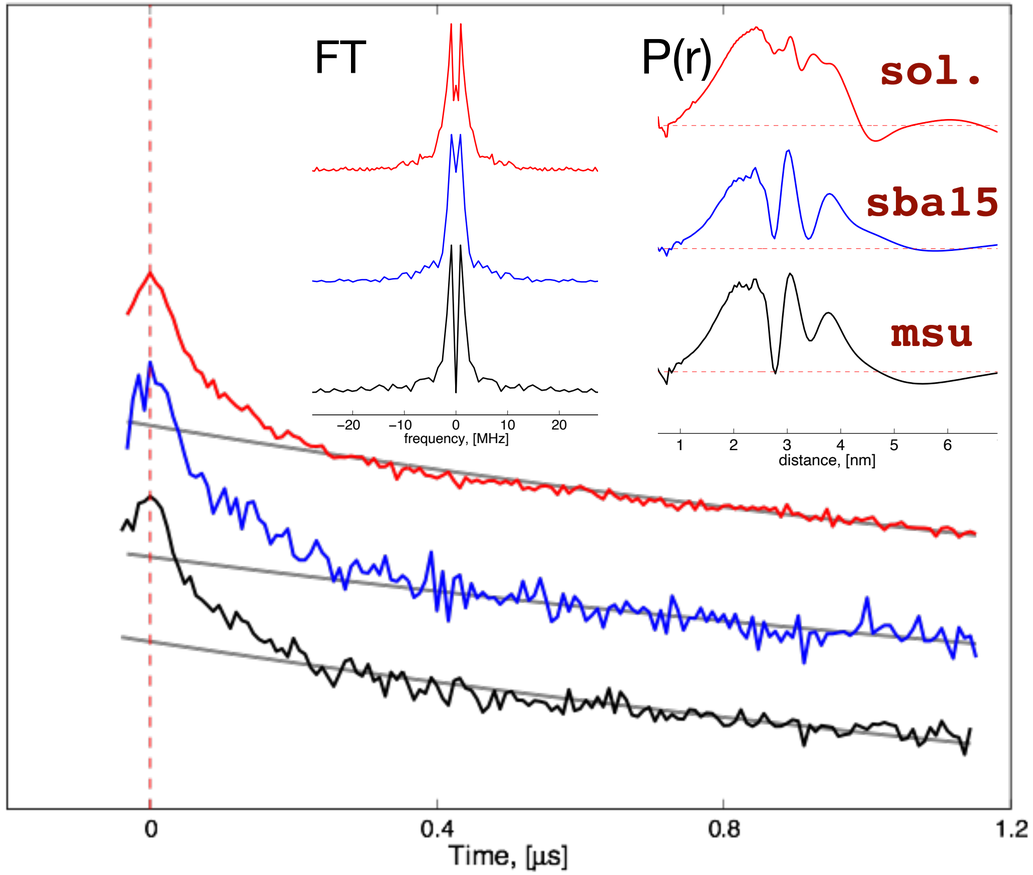

- CD shows PPII structure is unchanged.
- ESR demonstrates the peptide structure is approximately the same in all conditions studies.
- **P(r) accuracy improved.**

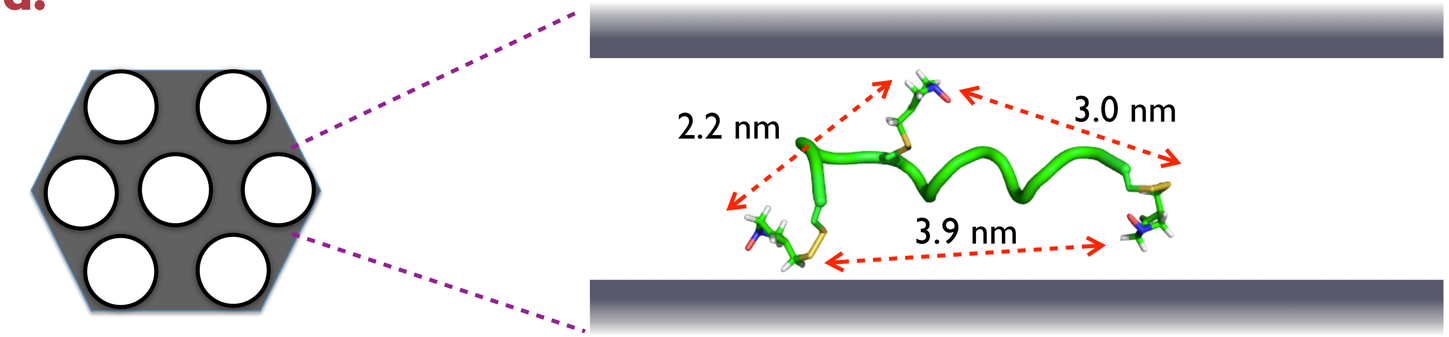

Theoretical Fits to Multifrequency Spectra

X-band (9 GHz)

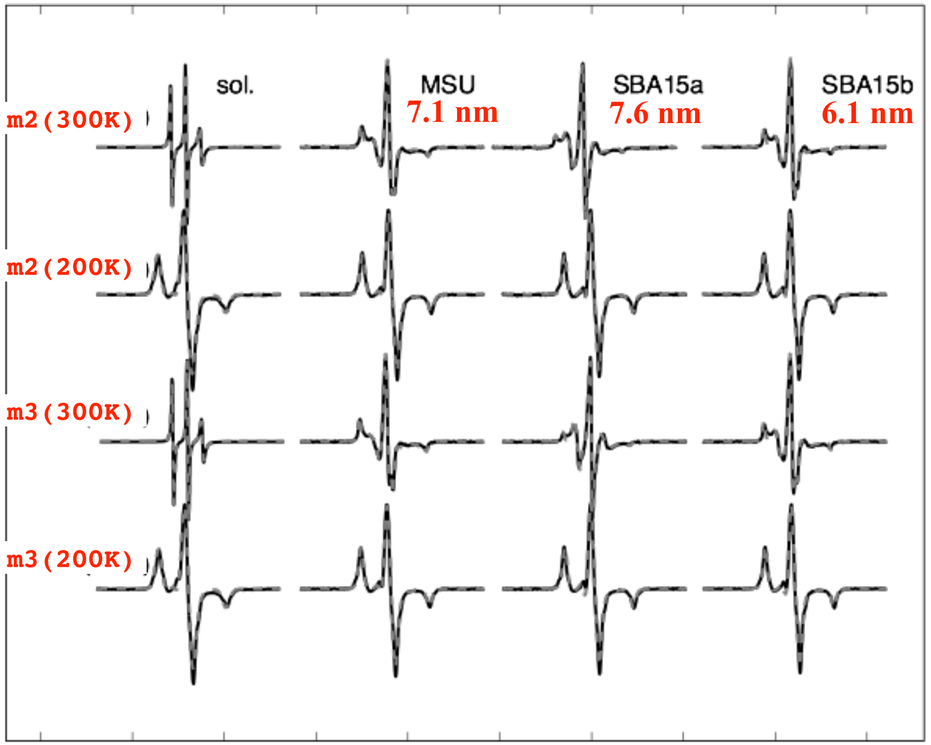

Q-band (35 GHz)

PP-m2 PPPPPPCPPPPPPP

PP-m3 PPPPPPPPCPPPPP

T = 300 K		$R_\perp$ (s^{-1})	$R_\parallel$ (s^{-1})	$R_\parallel/R_\perp$	S_0	$\Delta^{(0)a}$	[Im]^b
sol.		2.35×10^8	6.54×10^7	0.28	0.03	0.5	100% (100%)
MSU	Im	1.27×10^6	1.24×10^7	9.76	0.56	2.7	48% (38%)
	Mb	3.82×10^7	3.82×10^7	1.00	0.15	2.1	
SBA15a	Im	1.27×10^6	3.79×10^7	11.22	0.54	3.0	47% (32%)
	Mb	6.39×10^7	6.39×10^7	1.00	0.16	1.7	
SBA15b	Im	1.06×10^6	1.03×10^7	9.72	0.48	2.4	45% (46%)
	Mb	4.39×10^7	4.38×10^7	0.99	0.14	1.4	
T = 200 K	$R_\perp$ (s^{-1})	$R_\parallel$ (s^{-1})	$R_\parallel/R_\perp$	S_0	$\Delta^{(0)d}$	$\Delta^{(2)e}$	
sol.	6.81×10^5	1.71×10^5	0.25	0.62	7.5 (7.4)	0 (0)	
MSU	$(0.13 \pm 0.03) \times 10^6$	$(8.15 \pm 0.50) \times 10^6$	62.7	0.58 ± 0.05	1.9 (1.2)	4.6 (4.5)	
SBA15a	^{c}	^{c}	^{c}	^{c}	1.4 (1.6)	2.6 (3.3)	
SBA15b	^{c}	^{c}	^{c}	^{c}	1.4 (1.8)	3.9 (3.7)	

Multifrequency Analyses Unravel the Rotational Anisotropy

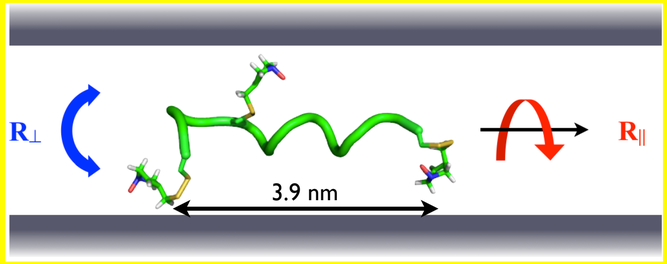

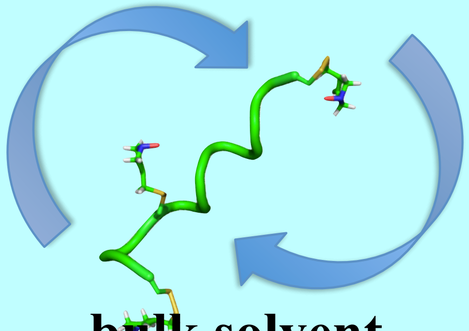

	Nanochannels (6, 7, 7,6 nm)	**bulk solvent**
$R_{\|\|}/R_{\perp}$	60 ← 10	0.26±0.02
S_0	0.54±0.04	0.62 ← 0.03
$\triangle^{(2)}$	3.6±1.0	~ 0
comp.	one ← two	one ← one
Temp	200 K — 300 K	200 K — 300 K

- Nano-confined molecules possess a greater **ordering** and anisotropy $R_{||}/R_{\perp}$ as compared to the bulk study.
- $R_{||}/R_{\perp}$ barely changes with pore sizes, as the nanoconfinement effects persist.

Significance of the Spectral Components

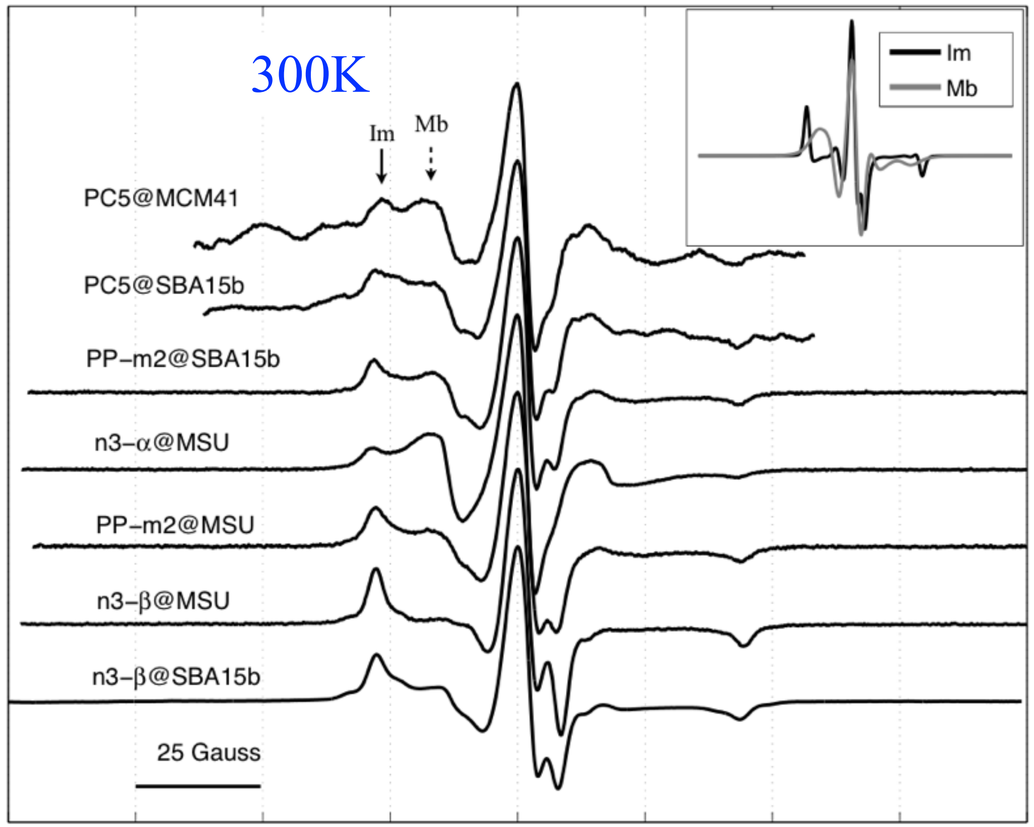

PC5

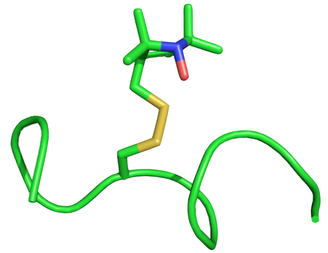

n3-α

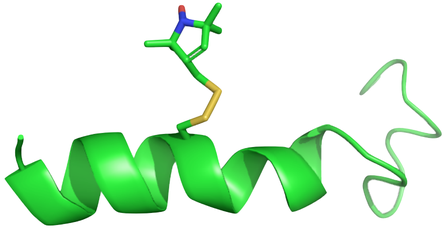

n3-β

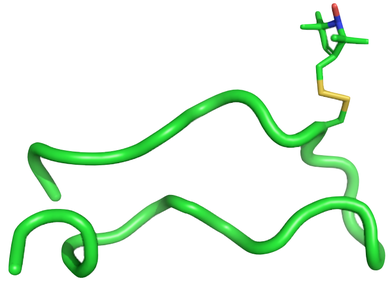

Mb reports

- *helical structural types (PPII or α-helix)* (X)
- *peptide length (11-, 14, or 26-aa long)* (X)
- *solvents (H_2O, PB, or TFE/PB)* (X)
- *pore sizes (2.5 ~7.6 nm)* (X)
- *backbone dynamics on secondary structures (helix vs. hairpin)* (O)

JACS
JOURNAL OF THE AMERICAN CHEMICAL SOCIETY
Cite This: J. Am. Chem. Soc. 2018, 140, 16032−16036
Commur
pubs.acs.

How Do Enzymes Orient When Trapped on Metal−Organic Framework (MOF) Surfaces?

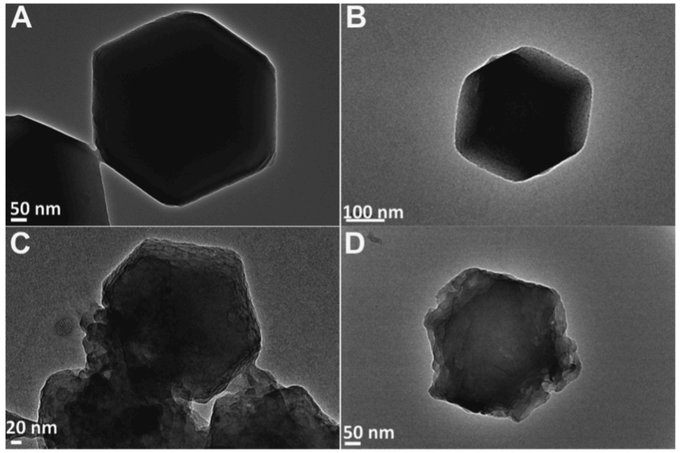

Figure 1. TEM images of ZIF-8 in MeOH (A) and PBS buffer (B) and hL/ZIF-8 composites in MeOH (C) and PBS buffer (D).

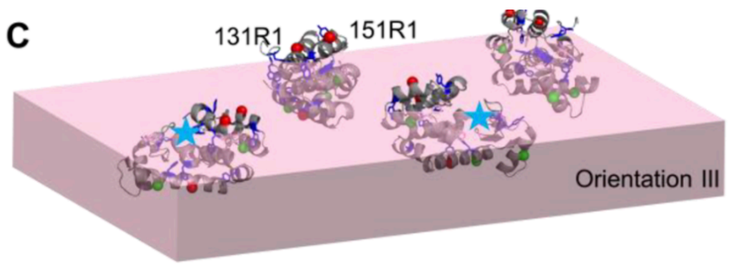

Red: residues more likely to be buried (72R1, 131R1, and 151R1);
Green: residues more likely to be exposed (44R1, 65R1, and 118R1);
Blue sticks: exposed aromatic residues;
Star: T4L active site; pink: ZIF-8 scaffold.

Figure 4. Proposed orientations of T4L on ZIF-8 crystal surface from four angles differing by 90° clockwise. For details of model construction and other possible orientations, see the SI.

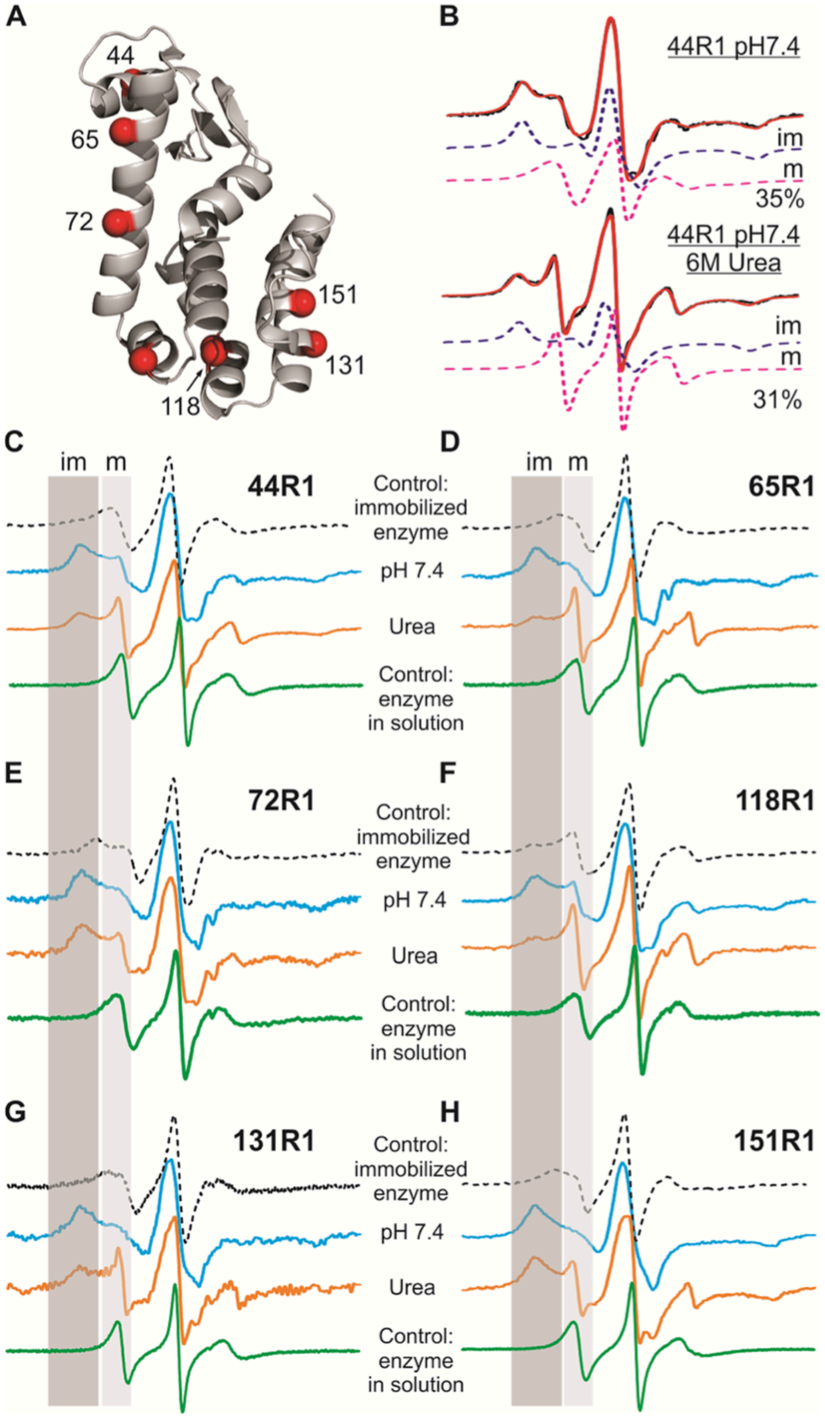

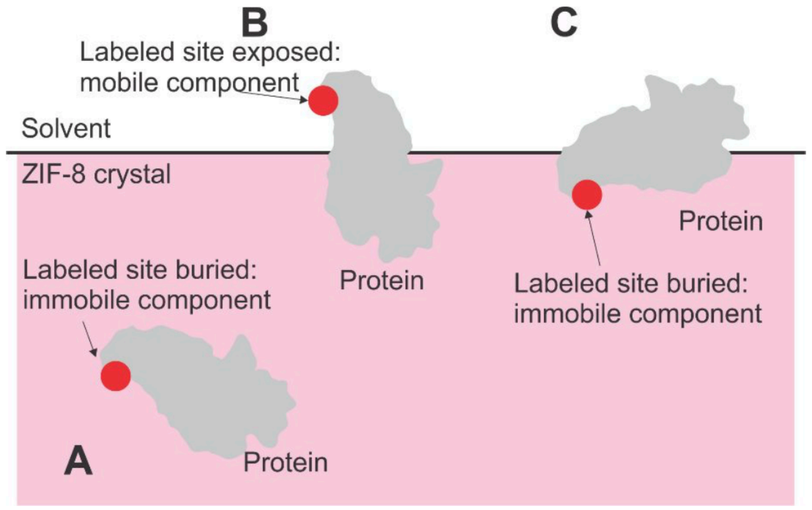

immobilized/trapped in MOFs due to the interferences of the MOF background signals. To address such challenge, we demonstrate in this work the utilization of site-directed spin labeling in combination with Electron Paramagnetic Resonance spectroscopy, which allows for the first time the characterization of the orientation of enzymes trapped on MOF surfaces. The obtained insights are fundamentally important for MOF-based enzyme immobilization design and understanding enzyme orientation once

Figure S6. Schematic illustration of EPR signal reporting both buried and solvent-exposed enzymes. Buried sites, either buried deep inside (A) or partially buried below the crystal surface (C) will contribute an immobile component to the EPR spectrum, while an exposed labeled site (B) will show a mobile component in the spectrum.

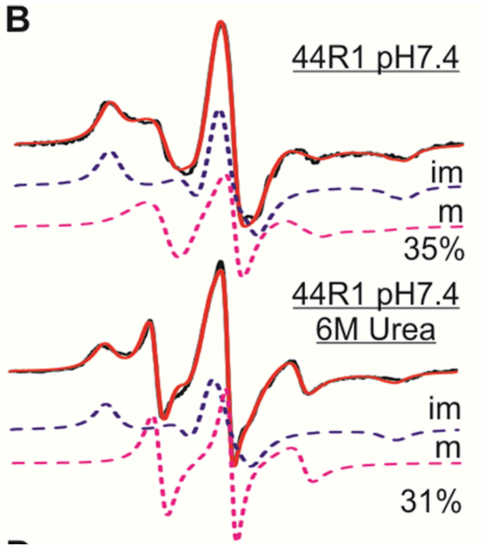

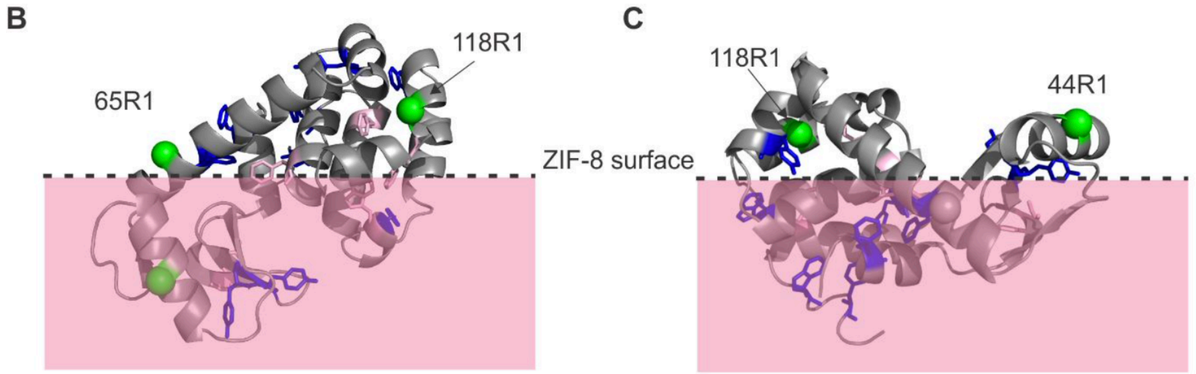

Figure S9. (A) An orientation to expose 44R1, 65R1, and 118R1 simultaneously. The buried portion (below the dotted line) is likely too small to trap the enzyme under the ZIF-8 crystal surface. (B) An orientation to expose 65R1 and 118R1. The buried portion is also too small to trap the enzyme under the ZIF-8 crystal surface. (C) It might be possible to simultaneously expose 44R1 and 118R because the buried portion is dominant.